

Science Reprint

The Amount of Recycled Crust in Sources of Mantle-Derived Melts

Alexander V. Sobolev, Albrecht W. Hofmann,
Dmitry V. Kuzmin, Gregory M. Yaxley,
Nicholas T. Arndt, Sun-Lin Chung,
Leonid V. Danyushevsky, Tim Elliott,
Frederick A. Frey, Michael O. Garcia,
Andrey A. Gurenko, Vadim S. Kamenetsky,
Andrew C. Kerr, Nadezhda A. Krivolutskaya,
Vladimir V. Matvienkov, Igor K. Nikogosian,
Alexander Rocholl, Ingvar A. Sigurdsson,
Nadezhda M. Sushchevskaya, Mengist Teklay

20 April 2007
Volume 316, pp.412-417

The Amount of Recycled Crust in Sources of Mantle-Derived Melts

Alexander V. Sobolev,^{1,2*} Albrecht W. Hofmann,¹ Dmitry V. Kuzmin,^{1,3} Gregory M. Yaxley,⁴ Nicholas T. Arndt,⁵ Sun-Lin Chung,⁶ Leonid V. Danyushevsky,⁷ Tim Elliott,⁸ Frederick A. Frey,⁹ Michael O. Garcia,¹⁰ Andrey A. Gurenko,¹ Vadim S. Kamenetsky,⁷ Andrew C. Kerr,¹¹ Nadezhda A. Krivolutskaya,² Vladimir V. Matvienkov,¹² Igor K. Nikogosian,^{13,14} Alexander Rocholl,¹⁵ Ingvar A. Sigurdsson,¹⁶ Nadezhda M. Sushchevskaya,² Mengist Teklay¹⁷

Plate tectonic processes introduce basaltic crust (as eclogite) into the peridotitic mantle. The proportions of these two sources in mantle melts are poorly understood. Silica-rich melts formed from eclogite react with peridotite, converting it to olivine-free pyroxenite. Partial melts of this hybrid pyroxenite are higher in nickel and silicon but poorer in manganese, calcium, and magnesium than melts of peridotite. Olivine phenocrysts' compositions record these differences and were used to quantify the contributions of pyroxenite-derived melts in mid-ocean ridge basalts (10 to 30%), ocean island and continental basalts (many >60%), and komatiites (20 to 30%). These results imply involvement of 2 to 20% (up to 28%) of recycled crust in mantle melting.

It is widely accepted that the heterogeneity of the convecting mantle observed in the composition of mantle-derived magmas is largely due to subduction and recycling of oceanic crust into the deep mantle (1, 2). To understand the role of crustal material in creating compositional heterogeneities in the mantle and to evaluate the geodynamical consequences of this contribution, one must quantify the crustal

input to the mantle sources of common, mantle-derived magmas in mid-oceanic ridges basalts (MORBs), ocean islands (OIBs), and large igneous provinces (LIPs). It is not possible to use incompatible element abundances in basalts to constrain the proportion of recycled component in the magma source because concentrations of these elements are also sensitive to the extent of melting. Similarly, the use of isotope ratios for making such quantitative estimates is compromised by the isotopic variability of subducted materials involved in the recycling process (2). We used an alternative approach based on a combination of major elements and compatible trace elements in parental melts, because these are more uniform in the mantle and are strongly controlled by the residual phases in equilibrium with partial melts (3–5).

Our method has its basis in the experimental and theoretical prediction that high-pressure ($P > 3.0$ GPa) melting of typical recycled oceanic crust (in the form of eclogite with a separate SiO_2 phase) and reaction of this melt with peridotite produces olivine-free pyroxenite (5). We show that further melting of this hybrid lithology in the absence of residual olivine is more voluminous than the melting of peridotite (at a given pressure and temperature) and that pyroxenite-derived melts are characteristically enriched in Si and Ni but depleted in Mg, Ca, and Mn compared with their peridotite-derived counterparts. This difference arises because olivine principally controls the composition of melt produced in peridotite, whereas pyroxene mainly controls the composition of melt from olivine-free hybrid pyroxenite (5–8). Experimental data predict (9) that, as such pyroxenite-derived melts rise toward the surface, the decrease in pressure causes their saturation in olivine. This olivine is unusually Ni rich and Mn and Ca poor. With use of a new, large data set of high-precision analyses of

olivine phenocrysts from OIBs, LIPs, MORBs, and komatiites, we show that hybrid pyroxenite is a common lithology in upwelling mantle and a major contributor to tholeiitic (silica-saturated) and transitional (moderately silica-undersaturated) magmas of OIBs and LIPs emplaced on thick oceanic or continental lithosphere.

Olivine data set. We use olivine phenocrysts as probes of parental melt composition, because olivine is the first phase to precipitate at low pressures in almost all mantle-derived magmas and because its forsterite content is an excellent measure of the degree of fractional crystallization allowing reconstruction of the parental melt composition.

Olivine phenocrysts were analyzed by electron microprobe using high probe currents and long counting times (10). This procedure routinely yields detection limits of around 6 to 15 parts per million (ppm) and errors (2 standard errors) of 15 to 30 ppm for trace elements (Ni, Ca, Mn, Cr, Co, and Al) and 0.01 mole percent (mol %) for forsterite content [defined as $\text{Fo} = \text{Mg}/(\text{Mg} + \text{Fe})$], checked by repeated analysis of San Carlos olivine standard (11). In the following diagrams we use only high-precision data.

We have analyzed nearly 17,000 grains of olivine phenocrysts from 229 samples of tholeiitic to transitional compositions covering MORBs (40 samples) from Mid-Atlantic Ridge, East Pacific Rise, South-East Indian Ridge, and Knipovich Ridge; OIBs (138 samples) from Hawaiian Islands and Emperor Seamounts, Canary Islands, Reunion, Azores, and Iceland; LIPs (36 samples) from Ontong Java Plateau, Siberia, Emeishan, Karoo, Afar, and North Atlantic Province; komatiites and associated picrites (15 samples) from the Archean Abitibi greenstone belt in Canada and the Belingwe belt in Zimbabwe and South Africa; Proterozoic komatiitic basalts from Gilmour Island, Canada; and komatiites and picrites from Gorgona Island, Colombia. Most samples are picrites or olivine basalts containing large amounts of fresh, high-magnesium olivine phenocrysts. The samples are subdivided into four groups: (i) MORB; (ii) within plate magmas (WPM, magmas erupted far from plate boundaries) forming OIB emplaced over thin lithosphere (<70 km thick), WPM-THIN; (iii) WPM (OIB and LIP) emplaced over thick lithosphere (>70 km thick), WPM-THICK; and (iv) komatiites and associated magmas, KOMATIITES. Details of sample locations, references for sample descriptions, and their group correspondence are presented in table S2a.

The most-magnesian olivine compositions (defined by olivines phenocrysts with Fo within 1 mol % from a maximum Fo) for each specimen were averaged (table S2a) for the plots shown in Fig. 1. Individual olivine analyses are presented on fig. S4 and tables S2, c to f.

In addition to Mn and Ni concentrations, which strongly correlate with Fo (Fig. 1, A and

¹Max Planck Institute (MPI) for Chemistry, Post Office Box 3060, 55020 Mainz, Germany. ²Vernadsky Institute of Geochemistry and Analytical Chemistry, Russian Academy of Sciences, Kosygin Street 19, 119991 Moscow, Russia. ³Institute of Geology and Mineralogy, Siberian Branch of Russian Academy of Sciences, Koptuyga prospekt 3, 630090 Novosibirsk, Russia. ⁴Research School of Earth Sciences, Australian National University, Canberra, ACT 0200 Australia. ⁵Laboratoire de Géodynamique des Chaînes Alpines, Université de Grenoble, 38401 Grenoble cedex, France. ⁶Department of Geosciences, National Taiwan University, Post Office Box 13-318, Taipei 106, Taiwan. ⁷Australian Research Council, Centre of Excellence in Ore Deposits and School of Earth Sciences, University of Tasmania, Private Bag 79, Hobart, Tasmania, 7001, Australia. ⁸Department of Earth Sciences, Queen's Road, Wills Memorial Building, University of Bristol, Bristol BS8 1RJ, UK. ⁹Department of Earth, Atmospheric, and Planetary Science, Massachusetts Institute of Technology (MIT), 77 Massachusetts Avenue, Cambridge, MA 02139, USA. ¹⁰Department of Geology and Geophysics, University of Hawaii, 1680 East-West Road, Honolulu, HI 96822, USA. ¹¹School of Earth, Ocean and Planetary Sciences, Cardiff University, Main Building, Park Place, Cardiff CF10 3YE, UK. ¹²P. P. Shirshov Institute of Oceanology of Russian Academy of Sciences, Nakhimovsky prospekt 36, 117997 Moscow, Russia. ¹³Department of Petrology, Faculty of Geosciences Utrecht University, Budapestlaan 4, Utrecht, Netherlands. ¹⁴Department of Petrology, Faculty of Earth and Life Sciences, Vrije Universiteit, De Boelelaan 1085, 1081 HV Amsterdam, Netherlands. ¹⁵Department of Earth and Environmental Sciences, University Munich, 80333 Munich, Germany. ¹⁶South Iceland Nature Centre, Strandvegur 50, Vestmannaeyjar, IS 900, Iceland. ¹⁷Department of Earth Science, University of Asmara, Asmara, Eritrea.

*To whom correspondence should be addressed. E-mail: sobolev@geokhi.ru

C), we also plot Mn/Fe and Ni versus Mg/Fe ratios (Fig. 1, B and D). These ratios do not vary significantly with olivine fractionation (see model curves Frac 1 and Frac 2) but nevertheless range considerably (Fig. 1, B and D). Most olivine phenocrysts from MORBs and many from komatiites have Mn and Ni contents similar to those of peridotite-derived melts. In contrast, most olivines from the WPM-THICK group are significantly depleted in Mn and enriched in Ni. Their concentrations are not compatible with the melting products of common peridotites. The olivines from the WPM-THIN group have intermediate Mn and Ni contents.

Concentrations of Ca also provide some discrimination in spite of the greater overlap. Most olivines from the WPM-THICK group are too low in Ca to have precipitated from peridotite-derived melts (shown as experimental-based model compositions and fractionation trajectories, Fig. 1E).

Chromium is strongly controlled by garnet and spinel in peridotites and thus might be useful to decipher products of high-degree melting of

peridotite, which leave residuals (restites) free of Cr-rich phases (12). Olivines from Archean komatiites have the highest Cr values and match compositions of olivines from a spinel- and garnet-free refractory restite (Fig. 1F). They could, therefore, be derived directly from high-degree melting of peridotite. In the other groups of olivines, Cr is markedly lower than expected in equilibrium with peridotite at high pressures (see experimental data on lherzolite melting, Fig. 1F). The lowest Cr contents are found in MORB olivines, indicative of residual Cr spinel.

Cobalt (Fig. 2A) shows nearly uniform correlation with Fo for all rock groups, with possibly only minor (around 5%) relative enrichment in WPM-THICK and WPM-THIN over MORB (estimated from group average Co/Fe of table S2a). Decoupling of Co and Ni yields Ni/Co ratios of many WPM-THICK olivines that are unusually high for the Earth mantle (Fig. 2B).

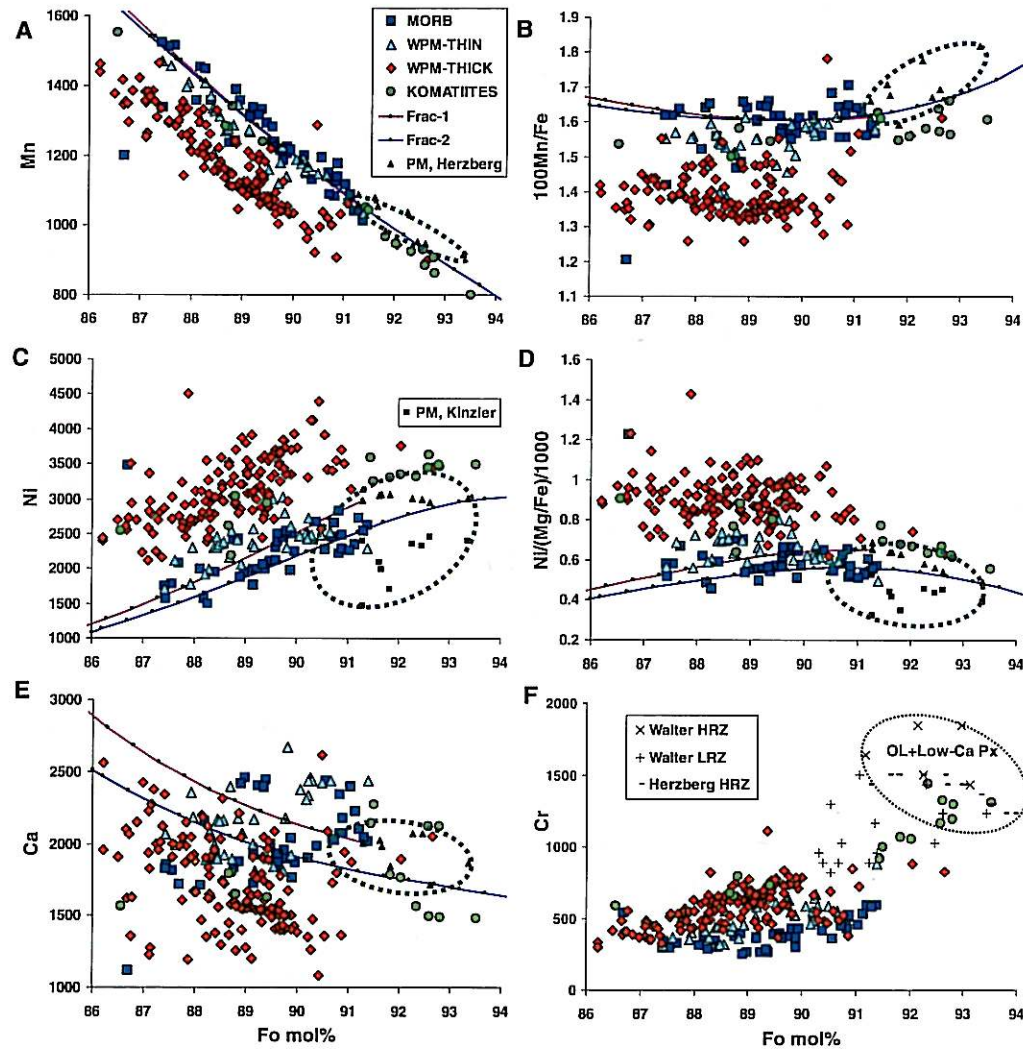
Mn/Fe is the parameter least dependent on olivine fractionation (as shown by the model fractionation curves in Fig. 3). Thus, it is diagnostic of parental magma compositional differ-

ences. There is a significant negative correlation of Ni/Mg versus Mn/Fe (linear correlation coefficient r is 0.66 for 238 samples) in spite of strong dependence of Ni/Mg on the degree of olivine fractionation (see fractionation trajectories in Fig. 3A). This correlation improves ($r=0.88$ for 103 samples) for the subset of olivines with a narrower range of Fo contents (Fo89 to Fo91). MORB olivines are the lowest in Ni and highest in Mn, whereas olivines from the WPM-THICK group are the highest in Ni and lowest in Mn, with olivines from the WPM-THIN group being intermediate.

To minimize the effects of olivine fractionation, we show parameters Ni/(Fe/Mg) and Ca/Fe in Fig. 3, B and C. This procedure also reduces the scatter in the ordinate significantly, thus highlighting the differences between geodynamic settings.

Fate of recycled oceanic crust. In subduction at $P > 2.5$ GPa, the basaltic and gabbroic portions of the oceanic crust are transformed completely to eclogite (clinopyroxene and garnet) with a free SiO₂ phase (13–15). Unless silica has been

Fig. 1. (A to F) Average compositions of the most highly magnesian olivine phenocrysts in each sample. Concentrations and their ratios are given in ppm versus forsterite content of olivine in mol %. Olivine group names are as defined in text. PM, Herzberg indicates compositions of olivine in equilibrium at 0.1 MPa with melt originally generated at 3.0 to 5.0 GPa from fertile peridotite (12), calculated by Petrolog software (41) for oxygen fugacity corresponding to quartz-fayalite-magnetite (QFM) buffer using the Herzberg model (4). PM, Kinzler, olivine compositions similar to PM, Herzberg but with Ni calculated by using Ni partitioning between olivine and melt from Kinzler *et al.* (28). Frac 1 is the trend of olivine composition during fractional crystallization from a melt derived from fertile peridotite at 3 GPa and 1515°C (12). Fractionation of olivine modeled up to 20% for oxygen fugacity corresponding to QFM buffer using the Herzberg model (4). Frac 2 is similar to Frac 1 but calculated for 35% crystallization of melt derived at 4.0 GPa and 1630°C (12). Green ellipse indicates field of olivine compositions compatible with peridotitic source. In (F), HRZ, Herzberg stands for calculated compositions of olivine from spinel- and garnet-free harzburgite restite using (4); LHRZ, Walter and HRZ, Walter indicate experimental olivines from lherzolite- and garnet-free harzburgite residual assemblages, respectively, produced by high-pressure melting of fertile peridotite (12). Black ellipse marked “ol + low Ca-Px” indicates field of olivine compositions from refractory garnet- and spinel-free assemblage of olivine and low-Ca pyroxene.



removed during subduction (16), this combination will also be the relevant assemblage during recycling to the upper mantle (17).

In the ascending mantle (e.g., a mantle plume or upstream flow of convecting mantle), the silica-oversaturated eclogite starts melting at higher pressures than the peridotite and produces high silica melt (18, 19). This melt reacts with olivine from peridotite, producing pyroxenes and garnet (5, 8, 19). Previous studies have envisioned that this reaction creates a refertilized peridotite enriched in pyroxene (19, 20). This conclusion would predict variable mixing proportions of individual ingredients (eclogite-derived high-Si melt and peridotite) that are

drastically different in composition. Melting such variable source compositions would create highly nonlinear correlations of $^{187}\text{Os}/^{188}\text{Os}$ and $^{87}\text{Sr}/^{86}\text{Sr}$ isotope ratios in the melts, and this is contradicted by the strongly linear correlations observed in Hawaiian basalts (21, 22), which are thought to have a significant eclogite component (3, 5).

However, it has been shown experimentally (23) and proposed on the basis of Korzinskii's theory (24) that, under conditions of local equilibrium, the reaction between high-Si eclogite-derived melt and peridotite produces an olivine-free lithology enriched in pyroxene (5). This fundamentally differs from a partial reaction (19, 20) because it leads to a stable pyroxenite lithology (hybrid py-

roxenite) generated by roughly fixed proportions of high-Si melt and peridotite [constrained by reaction stoichiometry between 40 and 60 weight % (wt %) of melt (5)] irrespective of the initial proportions of the reaction ingredients. Consequently, the hybrid pyroxenite has nearly uniform chemical and isotopic composition, thus constituting a single mixing endmember. Binary mixing of melts derived from peridotite and this pyroxenite leads to near-linear $^{87}\text{Sr}/^{86}\text{Sr}$ versus $^{187}\text{Os}/^{188}\text{Os}$ trends (5).

Other predicted geochemical consequences of replacement of olivine by pyroxene are a significant decrease of the bulk distribution coefficient between crystals and melt (K_d) for Ni

Fig. 2. (A and B) Cobalt and nickel to cobalt ratio versus Fo of average Mg-rich olivine phenocrysts. Pink band at $\text{Ni}/\text{Co} 20 \pm 1$ represents estimated values for bulk silicate Earth (BSE), core, and chondrites (39). Arrows indicate trend of olivine compositions due to the mantle melting (melting) and magma crystallization (cryst). All other symbols are as on Fig. 1.

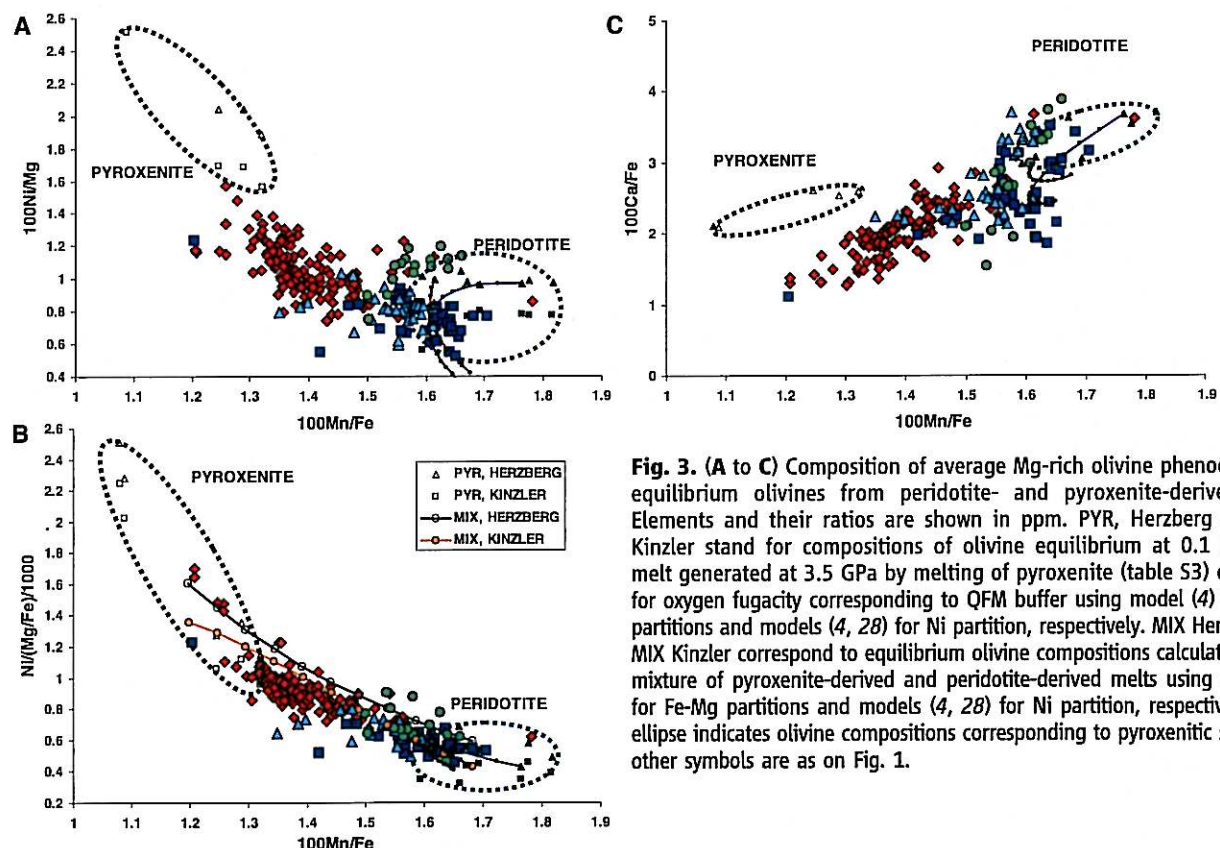
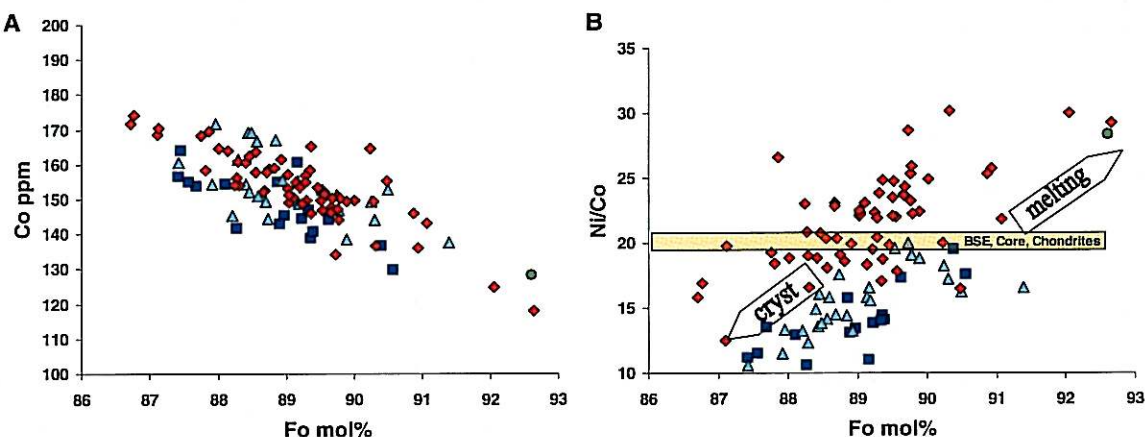


Fig. 3. (A to C) Composition of average Mg-rich olivine phenocrysts and equilibrium olivines from peridotite- and pyroxenite-derived melts. Elements and their ratios are shown in ppm. PYR, Herzberg and PYR, Kinzler stand for compositions of olivine equilibrium at 0.1 MPa with melt generated at 3.5 GPa by melting of pyroxenite (table S3) calculated for oxygen fugacity corresponding to QFM buffer using model (4) for Fe-Mg partitions and models (4, 28) for Ni partition, respectively. MIX Herzberg and MIX Kinzler correspond to equilibrium olivine compositions calculated for the mixture of pyroxenite-derived and peridotite-derived melts using model (4) for Fe-Mg partitions and models (4, 28) for Ni partition, respectively. Black ellipse indicates olivine compositions corresponding to pyroxenitic source. All other symbols are as on Fig. 1.

(5, 6) and a decrease in the ratio of the bulk coefficients of Mn and Fe (7). These features occur because olivine is the major silicate phase in peridotite concentrating Ni and the only silicate phase in peridotite having K_d for Fe greater than K_d for Mn (7). The bulk K_d changes will increase Ni and lower the Mn/Fe ratio of pyroxenite-derived melt compared with peridotite-derived melts. In addition, melting of pyroxenite yields lower Ca compared with peridotite (8). Additional predicted differences are higher melt fractions for hybrid pyroxenite than peridotite and higher Si and lower Mg in pyroxenite-derived melt (5, 25, 26).

These predictions were tested by experimental melting of a model hybrid pyroxenite (5). Experiments were run at $P = 3.5$ GPa and temperatures between 1400° and 1570°C in a conventional 1.27-cm piston-cylinder apparatus at the Australian National University (10, 19). These results, together with published experimental data for melting of peridotite (12), confirm the Ni and Mn relationships as well as melting rates predicted above (table S3 and fig. S5). From these data, we calculate equilibrium olivine compositions at low pressure (4, 27, 28) in order to compare them with the natural phenocryst data (Fig. 3). We used these results to estimate mixing proportions of melts derived from the two end-member sources for the olivine data sets representing different geodynamic settings. The end-member melt compositions were calculated from averaging experimental data on melting of pyroxenite and peridotite (10).

Quantitative estimates. We assumed mixtures (in 10% intervals) of the end-member melts (10) and calculated the composition of equilibrium olivines. The calculated mixing trajectories for the two different models for Ni partitioning

are consistent with natural olivine data (Fig. 3B). The relation between Mn/Fe of modeled olivines and mixing proportions (10) was used to compute the amount of pyroxenite-derived component for individual samples (Fig. 4). Olivines from the WPM-THICK group of basalts yield an average of $61 \pm 16\%$ (standard deviation) pyroxenite-derived component, similar to results derived from Ni contents in Hawaiian melt inclusions and olivines only (5). The olivines from some continental LIPs (specific suites from Siberia and Karoo) indicate almost pure pyroxenitic sources. Corresponding results for the other groups are for WPM-THIN, $30 \pm 13\%$; for Archean komatiites, $21 \pm 10\%$; and for MORB, excluding one unusual sample from the Southern Atlantic (see below), $17 \pm 12\%$ [similar to predictions of (25)]. Because of the uncertainties involved in estimating the end-member compositions, the differences between groups are better constrained than the absolute numbers. Although MORBs contain the lowest proportion of pyroxenite-derived melt, the spread of MORB data is significant, and many samples do contain substantial amounts of pyroxenite-derived component [the extreme is the enriched in silica MORB sample from the Southern Atlantic (29) with 100% pyroxenite-derived component]. The calculations show that the Archean komatiites contain a significant amount of pyroxenitic component (maximum of 30% for samples from Canada and Belingwe), although the largest amount is in Proterozoic komatitic basalts from Gilmour Island, Canada (up to almost 40%). From these calculations, an estimate of the amount of recycled oceanic crust (10) yields 4% for MORB, 11% for WPM-THIN group, 16% for WPM-THICK group, and around 13% for Archean komatiites. The highest estimate of

the amount of recycled oceanic crust (10) yield Ontong Java high-Mg lavas: 13% to 28%.

Silica-undersaturated basalts. Most of the magmas analyzed in this study are silica saturated (tholeites or transitional). Only a few samples are moderately silica-undersaturated alkali magmas (e.g., Azores and Afar). Our database is representative of the normal oceanic crust, several of the world's major suites of flood basalts (LIPs), several of the major modern mantle plumes (30), and some komatiites. The strongly silica-undersaturated associations not covered here include continental rift basalts, many smaller ocean islands consisting mostly of alkali lavas, and also some larger-flux plumes (30) such as Pitcairn, Tahiti, and Cape Verde islands. Why are such basalts that are highly enriched in incompatible elements, and therefore presumably generated by very low degrees of melting, nearly always undersaturated in silica? This observation appears to contradict our model; one would expect that silica-saturated melts generated from hybrid pyroxenites should be prevalent, especially at very low melt fractions. There are several possible explanations. (i) A volatile (mostly CO_2) triggered melting of peridotite may be the dominant mechanism forming strongly silica-undersaturated alkaline magmas at temperatures lower than hybrid pyroxenite melts (31). (ii) Low-degree melts of silica-saturated eclogite may be retained in the source because of their high viscosity, thus preventing production of the hybrid pyroxenite (5). (iii) Melting of hybrid pyroxenite at the contact with peridotite may produce low-degree, silica-undersaturated melts at lower temperatures than melting of hybrid pyroxenite itself (8). (iv) Melting of bimimetic eclogites (no free silica phase) formed from silica-undersaturated recycled crust produces undersaturated alkaline magmas (16).

What controls the amount of pyroxenite-derived melt? By following the method outlined above, we estimated the proportions of melt derived from pyroxenite and peridotite for each parental magma. These proportions depend on several interrelated parameters, namely the thickness of lithosphere, the potential mantle temperature (T_p) (32), and the amount of recycled crust in the upwelling mantle (Fig. 5). Because at the same T_p pyroxenite melts at higher pressure than peridotite (26), a thick lithosphere (which imposes a high lower limit on the depth of melting) will suppress low-depth peridotite melting and therefore favor a high proportion of pyroxenite-derived melts (33, 34). The extreme case is found in some continental flood basalts (specific suites of Siberia and Karoo at table S2a) where the amount of pyroxenite-derived melt is nearly 100%. In such a case, the amount of recycled material cannot be estimated because the peridotitic component contributes no melt. In contrast, a thin lithosphere (MORB, Iceland, Azores, and Detroit seamount) favors a higher proportion of peridotite-derived melt because of the increasing degree of melting of peridotite at shallower depths.

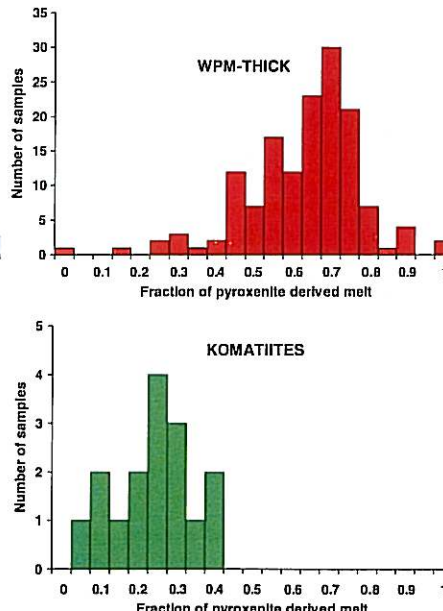


Fig. 4. Estimated amounts of pyroxenite-derived component in the parental melt for 229 samples of four different groups.

A high T_p is an important condition to maintain sufficient buoyancy of mantle plumes or any other upstream mantle flow, and this buoyancy limits the amount of dense eclogite that they can carry (35). Also, a high T_p affects mostly the proportion of peridotite-derived melt because fractional melting imposes a rather stringent upper limit to further melting at high melt fractions (36). High melt fractions are restricted to the eclogite and hybrid pyroxenite assemblages (26) (fig. S5). The peridotite assemblage produces lower melt fractions than pyroxenite (fig. S5) or eclogite (19, 25) at any given temperature and pressure, and its actual extent of melting therefore depends strongly on the specific T_p .

Lastly, why are the proportions of recycled component lower beneath mid-ocean ridges than in thick-lithosphere settings? We suggest several explanations: (i) Relatively low amount of dense recycled component in MORBs is limited by their T_p , which is too low to carry more. (ii) For statistical reasons, plumes are more likely to encounter more-common thick lithosphere than less-common thin lithosphere and few plumes impinge directly on ridges, so we are forced to deal with very-small-number statistics. (iii) Detroit seamount represents one case where a (Hawaiian) plume has encountered thin lithosphere and where our results do indicate a high fraction of recycled crust, similar to those found on the island of Hawaii on the thick lithosphere.

This amount is significantly higher than for Iceland, probably reflecting the effect of a higher T_p of the Hawaiian plume (4). (iv) The surface expression of a plume emplaced under thick lithosphere requires high T_p , which is necessary for carrying a significant amount of recycled crust (35), allowing melts to form at higher pressures than for ordinary peridotite (5, 25, 26), and melting a peridotite at higher pressures [e.g., komatiites (37)].

Heterogeneous versus homogeneous mantle. The model presented here assumes that the recycled crustal component was not fully mixed with peridotite during subduction and mantle convection and thus that the formation of the olivine-free hybrid lithology may take place. On the other hand, homogenization of crustal material within the peridotite mantle should create a range of ultramafic lithologies with variable amounts of olivine, similar to a model by Kelemen *et al.* (20). Under these circumstances, the major-element contents of partial melts will correspond to the eutectic-like composition, buffered by the peridotite assemblage, whereas the compatible trace elements (Ni and Mn) will be controlled by the bulk partition coefficients of this assemblage and thus by the amount of olivine and pyroxene present in the system. Therefore, the amount of recycled crust can still be estimated on the basis of these trace elements, but their abundances will no longer correlate with the

buffered major elements (Si, Ca, and Al). For Hawaiian basalts, such correlations with Ni are present (5), which requires a strongly heterogeneous source.

Input from Earth's core? The Ni excess in mantle olivines from Siberian LIP (38) and the elevated Fe/Mn ratios in Hawaiian lavas (7) have been explained by input from Earth's core to the sources of mantle plumes. This suggestion is consistent with $^{186}\text{Os}/^{188}\text{Os}$ ratios for some Hawaiian and Gorgona lavas (39) but is contradicted by the fact that concentrations of highly siderophile (Pt) and chalcophile (Cu) elements reported for Hawaiian basalts are not affected by this process (5). Our olivine data provide strong arguments against any notable core contribution to Ni or Fe excess in the sources of mantle-derived magmas. Cobalt does not show significant excess in olivines (Fig. 2 and fig. S3) and is effectively decoupled from Ni. As a result, the Ni/Co ratio in most Ni-rich mantle plume olivines exceeds 30 at the typical mantle Fo range of 89 to 91 (Fig. 2). This is not expected from a core contribution, because Ni/Co ratios for both mantle and core are almost equal and close to the chondritic value of about 20 (40). In addition, Ca is significantly depleted in many high-Ni and low-Mn olivines from the WPM-THICK group, which cannot be explained by core contribution. Lastly, the olivines from Gorgona komatiites, which do show significant excess in ^{186}Os (39), do not indicate large anomalies in Ni and Mn/Fe, whereas Koolau lavas with the highest Ni excess and lowest Mn/Fe ratio in olivines do not show significant elevations in $^{186}\text{Os}/^{188}\text{Os}$ ratios (39). This suggests complete decoupling of these potentially strong indicators of core-mantle exchange.

References and Notes

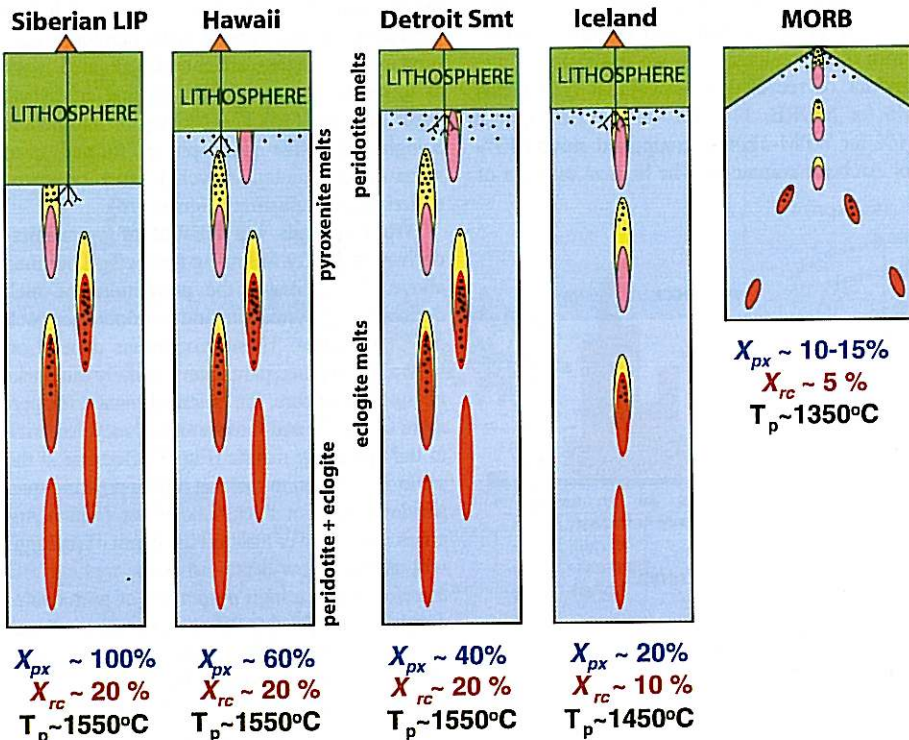


Fig. 5. Schematic model illustrating interplay between amount of recycled crust, thickness of lithosphere, and T_p . Blue, upwelling peridotitic mantle; red, recycled oceanic crust (eclogite with free SiO_2 phase); black dots, melting; yellow, reaction zones forming hybrid pyroxenite; pink, refractory restite after eclogite melting; and green, lithosphere. X_{px} , amount of pyroxenite derived melt in the mixture with peridotite-derived melt, and X_{rc} , amount of recycled oceanic crust in the peridotitic mantle (42).

1. A. W. Hofmann, W. M. White, *Earth Planet. Sci. Lett.* **57**, 421 (1982).
2. A. W. Hofmann, in *The Mantle and Core*, vol. 2 of *Treatise on Geochemistry*, H. D. Holland, K. K. Turekian, Eds. (Elsevier, Amsterdam, 2003), p. 61.
3. E. H. Hauri, *Nature* **382**, 415 (1996).
4. C. Herzberg, M. J. O'Hara, *J. Petrol.* **43**, 1857 (2002).
5. A. V. Sobolev, A. W. Hofmann, S. V. Sobolev, I. K. Nikogosian, *Nature* **434**, 590 (2005).
6. Ni was first proposed as a monitor for replacement of olivine by pyroxene in (20).
7. M. Humayun, L. P. Qin, M. D. Norman, *Science* **306**, 91 (2004).
8. C. Herzberg, *Nature* **444**, 605 (2006).
9. S. M. Eggins, *Contrib. Mineral. Petrol.* **110**, 387 (1992).
10. Materials and methods are available on *Science Online*.
11. E. J. Jarosevich, J. A. Nelen, J. A. Norberg, *Geostand. Newslett.* **4**, 43 (1980).
12. M. J. Walter, *J. Petrol.* **39**, 29 (1998).
13. V. S. Sobolev, A. V. Sobolev, *Dokl. Akad. Nauk SSSR* **237**, 437 (1977).
14. T. Kogiso, M. M. Hirschmann, D. J. Frost, *Earth Planet. Sci. Lett.* **216**, 603 (2003).
15. T. Kogiso, M. M. Hirschmann, M. Pertermann, *J. Petrol.* **45**, 2407 (2004).
16. T. Kogiso, M. Hirschmann, *Earth Planet. Sci. Lett.* **249**, 188 (2006).
17. A. Yasuda, T. Fujii, K. Kurita, *J. Geophys. Res.* **99**, 9401 (1994).
18. A. E. Ringwood, D. H. Green, *Tectonophysics* **3**, 383 (1966).

19. G. M. Yaxley, D. H. Green, *Schweiz. Mineral. Petrogr. Mitt.* **78**, 243 (1998).
20. P. B. Kelemen, S. R. Hart, S. Bernstein, *Earth Planet. Sci. Lett.* **164**, 387 (1998).
21. E. H. Hauri, M. D. Kurz, *Earth Planet. Sci. Lett.* **153**, 21 (1997).
22. J. C. Lassiter, E. H. Hauri, *Earth Planet. Sci. Lett.* **164**, 483 (1998).
23. R. P. Rapp, N. Shimizu, M. D. Norman, G. S. Applegate, *Chem. Geol.* **160**, 335 (1999).
24. D. S. Korzhinskiy, *Theory of Metasomatic Zoning* (Clarendon, Oxford, 1970).
25. M. M. Hirschmann, E. M. Stolper, *Contrib. Mineral. Petro.* **124**, 185 (1996).
26. G. M. Yaxley, *Contrib. Mineral. Petro.* **139**, 326 (2000).
27. P. Beattie, *Contrib. Mineral. Petro.* **115**, 103 (1993).
28. R. J. Kinzler, T. L. Grove, S. I. Recca, *Geochim. Cosmochim. Acta* **54**, 1255 (1990).
29. V. S. Kamenetsky et al., *Geology* **29**, 243 (2001).
30. N. H. Sleep, *Annu. Rev. Earth Planet. Sci.* **20**, 19 (1992).
31. G. H. Gudfinnsson, D. C. Presnall, *J. Petrol.* **46**, 1645 (2005).
32. D. McKenzie, M. J. Bickle, *J. Phys. Earth* **38**, 511 (1990).
33. J. P. Morgan, *Geochim. Geophys. Geosystems* **2**, 2000GC000049 (2001).
34. G. Ito, J. J. Mahoney, *Earth Planet. Sci. Lett.* **230**, 29 (2005).
35. M. Pertermann, M. M. Hirschmann, *J. Petrol.* **44**, 2173 (2003).
36. I. Kushiro, *Annu. Rev. Earth Planet. Sci.* **29**, 71 (2001).
37. N. Arndt, *J. Geophys. Res.* **108**, XX (2003).
38. I. D. Ryabchikov, *Dokl. Earth Sci.* **389**, 437 (2003).
39. A. D. Brandon, R. J. Walker, *Earth Planet. Sci. Lett.* **232**, 211 (2005).
40. W. F. McDonough, S. S. Sun, *Chem. Geol.* **120**, 223 (1995).
41. L. V. Danyushevsky, *J. Volcanol. Geotherm. Res.* **110**, 265 (2001).
42. D. McKenzie, M. J. Bickle, *J. Petrol.* **29**, 625 (1988).
43. We thank B. Schulz-Dobrick for supervising purchase and establishing electron microprobe facility in MPI; Hawaiian Scientific Drilling Project team, Koolau Scientific Drilling Project team, Ocean Drilling Program team, A. T. Anderson, E. A. Mathez, and N. Gitahi for providing samples; E. J. Jarosevich for supplying microprobe standards; A. Yasevich for sample preparations and N. Groschopf for maintaining the electron microprobe. The paper benefited from discussions with M. Hirschmann, P. Kelemen, C. Herzberg, B. McDonough, I. Ryabchikov, L. Kogarko, A. Kadik, E. Galimov, V. Batanova. Constructive reviews of C. Herzberg, and P. Kelemen improved the

clarity of the manuscript. The study was supported by Wolfgang Paul Award of the Alexander von Humboldt Foundation, Germany, to A.V.S. Partial support from the following sources is also acknowledged: Russian Foundation for Basic Research (RFBR) grants 06-05-65234 and НШ-4264.2006.5 and Russian Academy of Sciences and Deutsche Forschungsgemeinschaft grant HO 1026/16-1 to A.V.S., RFBR grant 06-05-64651 to N.M.S., NSF grants EAR03-36874 to M.O.G. and EAR-0105557 to F.A.F., and Netherlands Research Center for Integrated Solid Earth Science grant 6.2.12 to I.K.N. This is School of Ocean and Earth Science and Technology, University of Hawaii, contribution no. 7104.

Supporting Online Material

www.sciencemag.org/cgi/content/full/1138113/DC1

SOM Text

Figs. S1 to S5

Tables S1 to S4

Data set

29 November 2006; accepted 16 March 2007

Published online 29 March 2007;

10.1126/science.1138113

Include this information when citing this paper.



Supporting Online Material for The Amount of Recycled Crust in Sources of Mantle-Derived Melts

Alexander V. Sobolev, Albrecht W. Hofmann, Dmitry V. Kuzmin, Gregory M. Yaxley, Nicholas T. Arndt, Sun-Lin Chung, Leonid V. Danyushevsky, Tim Elliott, Frederick A. Frey, Michael O. Garcia, Andrey A. Gurenko, Vadim S. Kamenetsky, Andrew C. Kerr, Nadezhda A. Krivolutskaya, Vladimir V. Matvienkov, Igor K. Nikogosian, Alexander Rocholl, Ingvar A. Sigurdsson, Nadezhda M. Sushchevskaya, Mengist Teklay

Published 29 March 2007 on *Science Express*
DOI: 10.1126/science.1138113

This PDF file includes:

- Materials and Methods
- Figs. S1 to S5
- Tables S1, S2a, S2b, and S3
- References

Other Supporting Online Material for this manuscript includes the following:
available at www.sciencemag.org/cgi/content/full/1138113/DC1

Table S2 (complete) as zipped file

The Amount of Recycled Crust in Sources of Mantle-Derived Melts

A. V. Sobolev, A. W. Hofmann, D. V. Kuzmin, G. M. Yaxley, N. T. Arndt, et al.

Supporting Online Material

Methods and Samples

Electron probe microanalysis. Olivine phenocrysts were analyzed for Si, Fe, Mg, Ca, Ni, Mn, Cr, Al and Co with a Jeol JXA 8200 electron probe at Max-Planck Institute of Chemistry. Each olivine grain was analyzed in the geometrical center at 20 kV accelerating voltage and probe current of 300 nA. A small olivine subset was analyzed at 30 kV and 200nA. Details of analytical conditions are presented in Table S1. These conditions have been found optimal to obtain best detection limits (see Fig S1). The intensity of the Co K α line was additionally corrected for overlap with the shoulder of FeK β second order line using the following linear equation established by analyzing Fe bearing standards free of Co:

$$\text{CoO}_c = \text{CoO}_m - 0.0011 \times \text{FeO}_m - 0.013. \quad [\text{S1}]$$

Where CoO_c and CoO_m , FeO_m -are corrected and measured values correspondingly.

The constant in equation [S1] was obtained from analyses of San Carlos olivine standard with known Co content (Table S1). Note that the linear approximation of equation [S1] may not be valid for highly Mg ($\text{Fo} > 93$) and low Mg ($\text{Fo} < 70$) olivines.

In addition San Carlos olivine standard USNM 111312/444 (S1) was run (3 points per each 30-50 measurement points) as an

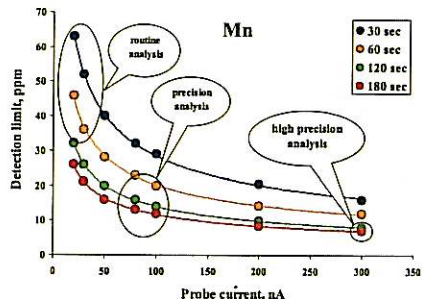


Fig. S1. Detection limit for Mn as function of probe current and peak counting time (in seconds, sec).

Detection limit was determined for San Carlos olivine standard with Jeol software using background statistics and 3 sigma criterion. Typical measurement conditions used in literature are marked as "routine analysis". Analysis at higher beam current and counting times published by (S3) is marked as "precision analysis". The analytical conditions used in this study are indicated as "high precision analysis".

unknown to monitor drifts in calibration and estimate accuracy of analysis. All measurements of Si, Fe, Mn, Ni, Ca and Al were corrected for deviation of this standard from the reference values (Table S1).

For trace elements, the above measurement conditions routinely yield detection limits of around 6-15 ppm based on 3 sigma criteria by Jeol standard software, and errors of 15-30 ppm for trace elements and 0.01 mol% for Fo content (2 standard errors) established by counting statistics and reproducibility of olivine standard (see Fig S1-S2). Precision and

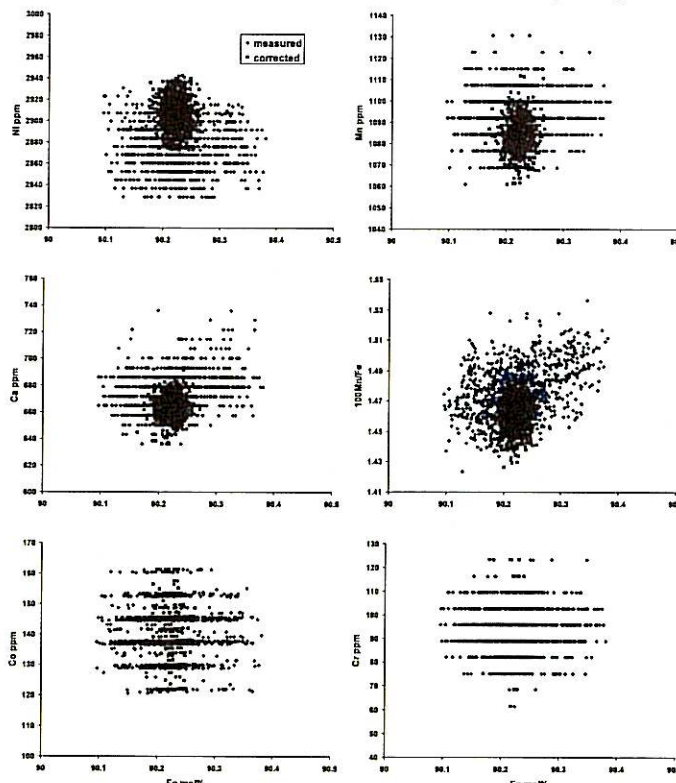


Fig. S2. Reproducibility of San Carlos olivine standard analyzed three times every 30 to 50-th measurement points. Measured- represent uncorrected measurements, corrected – stands for measurements corrected for the calibration drift.

Table S1. Typical analytical conditions of electron probe microanalysis of olivine. Probe current 300 nA, acceleration voltage 20kV.

El	St	Cryst	Line	Peak	BG(+)	BG(-)	S.C.O.
Si	1	TAP	K α	90	90	-	190740 *
Al	2	TAP	K α	240	120	120	170 #
Fe	1	LIF	K α	90	90	-	74230 *
Mn	3	LIFII	K α	120	60	60	1084 *
Mg	1	TAP	K α	90	45	45	298040 *
Ca	4	PETJ	K α	120	60	60	665 #
Ni	5	LIF	K α	150	70	70	2907 *
Co	6	LIFII	K α	120	120	-	140 **
Cr	7	PETJ	K α	120	60	60	95 #

Notes for Table S1: Standards (St) - 1- San-Carlos olivine USNM 111312/444 (S.C.O.); 2-pure Al₂O₃; 3-Rhodonite; 4-Wollastonite; 5-pure NiO; 6- pure Co-metal; 7-pure Cr₂O₃. Peak and background (BG) counting time in seconds. *-Accepted values for (S.C.O.) from ref (S1) in ppm, **-value measured by LA-ICP MS.

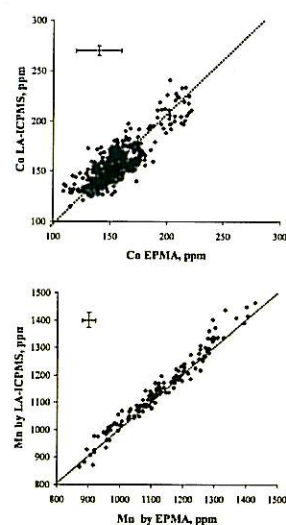


Fig. S3. Comparison between Co and Mn concentrations in olivine measured by EPMA and LA-ICPMS. Error bar corresponds to ± 2 standard errors for both EPMA and LA-ICP MS

accuracy of Co and Mn measurements were independently checked by LA-ICP MS analysis using Thermo Finnigan Element 2 mass spectrometer and New Wave Up213 YAG laser (213 nm wavelength) setup. KL2-G (S4) and NIST 612 glasses were used as a external standards and Ca in olivine as reference value. Figure S3 shows that both Co

and Mn concentrations measured by EPMA correspond to those analyzed by LA-ICP MS within 20 ppm (2 standard errors).

Olivine database. The averaged most highly magnesian olivines for each sample are presented in Table S2a. Individual olivine analyses are presented on Fig S4 and in Tables S2c,d,e,f separately for each group: MORB in Table S2c, WPM-THIN in Table S2d, WPM-THICK in Table S2e and KOMATIITES in

Table S2f. These tables are included as separate spreadsheets together with Table S2a in the Excel file called Table S2. Table S2a is also placed in the end of this file. Tables S2c,d,e,f include concentrations of oxides and their relative standard deviations in % (signal counting statistics) for individual olivine grains. Each analytical point in addition to

Melting of pyroxenites. The model hybrid pyroxenite composition from Sobolev et al. (S3) (their Table S2, column 50%) was chosen for the high pressure experimental investigation. A synthetic starting material with this composition (Px-1) was prepared for the experiments by blending high purity oxides and carbonates under analytical grade

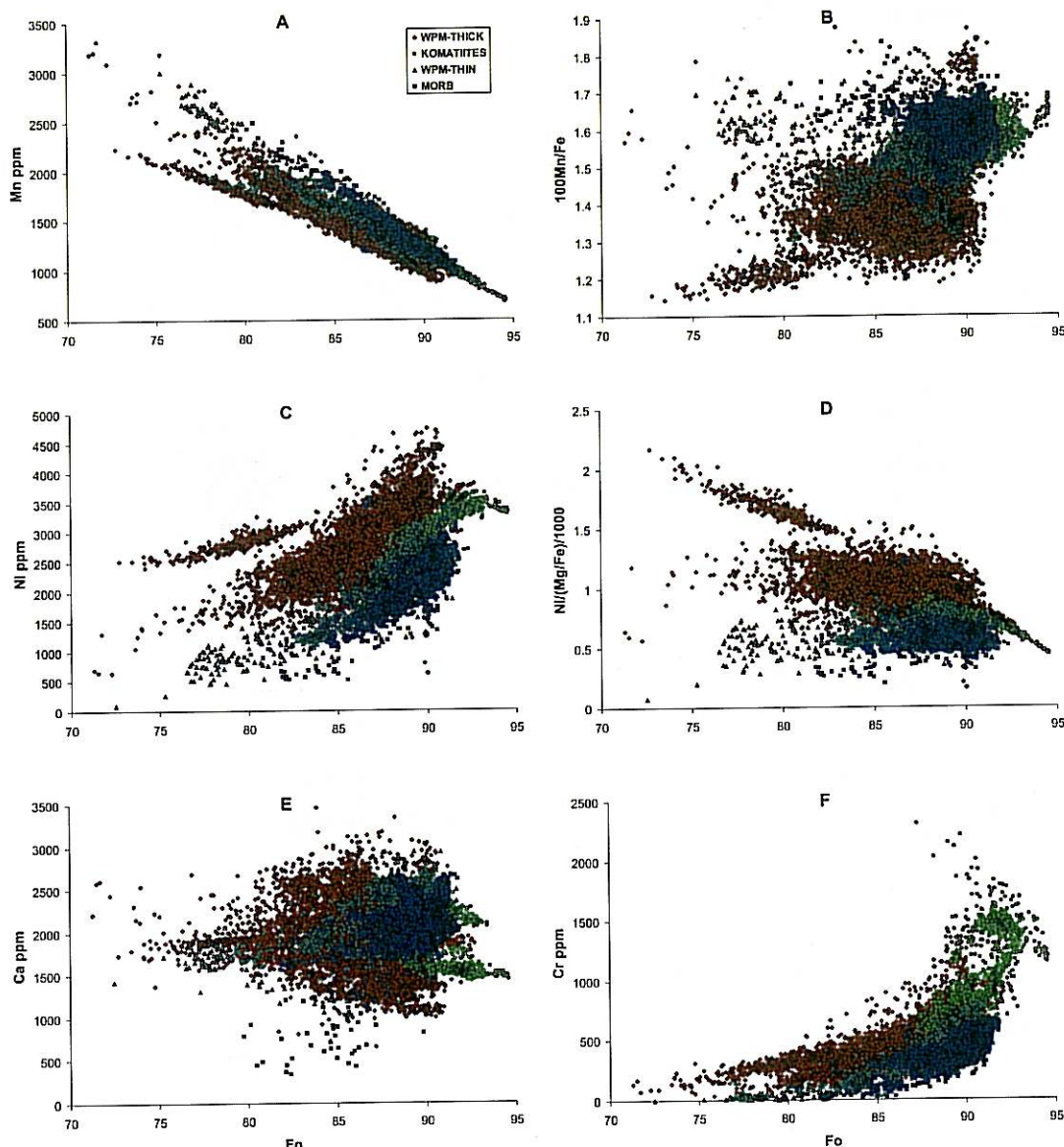


Fig. S4. Composition of olivine phenocrysts: all data from database. Group of MORB olivines shown on top of all groups.

and Mn concentrations measured by EPMA correspond to those analyzed by LA-ICP MS within 20 ppm (2 standard errors).

Olivine database. The averaged most highly magnesian olivines for each sample are presented in Table S2a. Individual olivine analyses are presented on Fig S4 and in Tables S2c,d,e,f separately for each group: MORB in Table S2c, WPM-THIN in Table S2d, WPM-THICK in Table S2e and KOMATIITES in

sample name has a unique number. Table S2a includes group title, sample name, reference for sample description (if published), information on locality, number of averaged high-Mg grains, forsterite content, element concentrations in ppm, standard errors of the mean in ppm, characteristic ratios of elements and calculated amount of pyroxenitic component (X_{px} , see below for explanation).

acetone for several hours, until the material was homogenous and very fine-grained. The resultant dried powder was then pelletised and fired for 12 hours at 1100°C to decarbonate and partially fuse the components. FeO was added after firing in the form of synthetic fayalite (Fe_2SiO_4), and again blended under acetone. The final mixture was then dried overnight at 200°C and subsequently stored at 110°C. The actual composition of the Px-1

starting material was checked by electron probe microanalysis of quenched glass prepared by fusing the starting mix at 1300°C in an Ar atmosphere in a box furnace and quenching in water (Table S3).

High pressure experiments were run at a pressure of 3.5 GPa and temperatures between 1400–1570°C in a conventional 1.27 cm piston-cylinder apparatus at the Australian National University. The Px-1 starting material (≈ 1 mg) was loaded into graphite capsules, which were sealed by arc-welding in Pt outer capsules. The

capsules were placed centrally into NaCl-pyrex sleeves with MgO inserts, an assembly which requires no friction correction. Type B thermocouples ($\text{Pt}_6\text{Rh}_{94}/\text{Pt}_{30}\text{Rh}_{70}$) were employed, with the thermocouple join placed within a fraction of a millimeter of the Pt capsule. Runs were brought to run temperature and pressure simultaneously. Temperature was controlled throughout by Eurotherm controllers attached to the thermocouple and is accurate to $\pm 10^\circ\text{C}$. Pressure is accurate to ± 0.1 GPa. Experiments were maintained at the

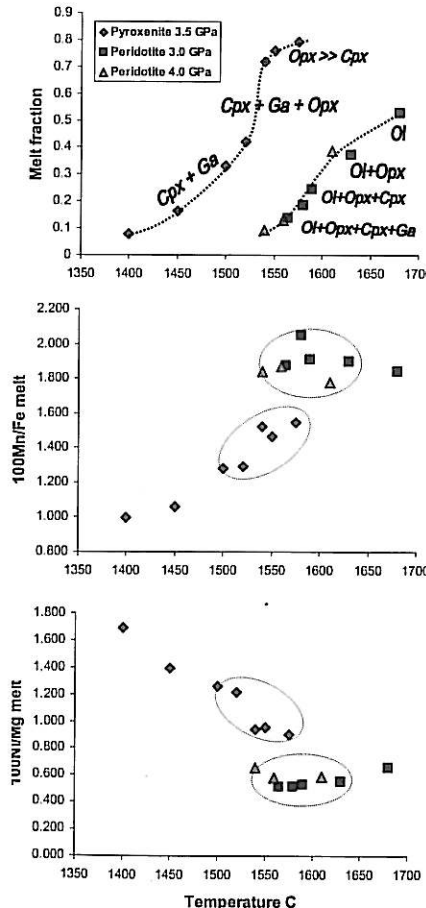
desired PT condition long enough to allow a close approach to equilibrium, and then quenched by terminating power to the furnace.

After recovery from the post-run assembly, the Pt capsules were mounted in 1 inch diameter epoxy buttons, sectioned longitudinally and polished, in preparation for analysis by scanning electron microscopy at the Australian National University and electron probe microanalysis at the Max Planck Institute for Chemistry in Mainz.

Table S3. Proportions of phases produced and melt compositions from melting of pyroxenite at 3.5 GPa and 1400–1575°C.

Run N	DT h	T °C	Phases proportions, wt%				Melt compositions in oxide wt%, Ni in ppm										
			melt	Opx	Cpx	Ga	SiO ₂	TiO ₂	Al ₂ O ₃	FeO	MnO	MgO	CaO	Na ₂ O	K ₂ O	Cr ₂ O ₃	Ni
C-2298	45	1400	8	0.	79	14	60.70	2.76	14.40	6.80	0.068	4.44	7.71	2.34	0.70	0.07	453
C-2317	48	1450	16	0	71	12	55.76	2.33	14.20	7.63	0.081	7.45	7.95	2.16	0.44	0.06	626
C-2301	5	1500	33	0	60	6	53.30	1.58	14.21	8.25	0.106	10.67	8.61	1.75	0.13	0.09	810
C-2330	5	1520	42	0	55	3	52.54	1.29	14.22	8.65	0.112	11.66	8.65	1.98	0.14	0.11	850
C-2332	5	1540	72	24	4	0	52.00	0.86	13.55	8.19	0.125	14.08	9.00	1.80	0.08	0.20	796
C-2318	6	1550	76	18	7	0	52.38	0.83	13.39	7.95	0.117	14.67	8.77	1.74	0.09	0.20	843
C-2319	5	1575	79	20	0	0	52.20	0.79	13.07	8.11	0.126	15.44	8.52	1.67	0.07	0.22	841
Px-1, Bulk composition							52.67	0.64	11.26	7.55	0.119	18.48	7.05	1.52	0.06	0.25	1000
Peridotite-derived endmember							46.79	0.85	11.50	9.68	0.185	19.07	10.00	0.84	0.47	0.39	642
Pyroxenite -derived endmember							52.56	1.07	13.71	8.24	0.117	13.32	8.72	1.79	0.10	0.16	830

Note for Table S3: Mell, Opx, Cpx, Ga, - proportions of melt, orthopyroxene, clinopyroxene and garnet in experimental runs in mass fractions, calculated using list square method from bulk composition and compositions of phases. DT- run duration in hours, T- temperature in °C. The amount of Ni has been calculated using the method described in Sobolev et al, 2005 (S3). This method uses known phase proportions and the distribution of Ni between phases, to calculate Ni in the phases on the basis of mass balance and known bulk Ni content. The assumed bulk Ni concentrations are: 1000 ppm for pyroxenite (Px-1) and 1900 ppm for peridotite (S3).



Pyroxenite-derived component in melts. In order to estimate endmember compositions we have averaged compositions of melts of pyroxenite and peridotite (see Fig.S5). For pyroxenite we averaged all melt compositions except numbers C-2298 and C-2327 (Table S3) produced at low temperature and low percentage of melting. For peridotites we averaged 7 compositions of melts from runs 30.12, 30.07, 30.14, 30.1 (3.GPa), 40.06, 40.07, 40.05 (4.GPa) of Walter, 1998 (S2). The endmember compositions are shown in Table S3. We assumed that the mixtures consist of endmembers with similar temperatures, and we therefore excluded (from the averaging procedure) experimental melts with very low or very high temperatures (see Fig.S5).

The calculated endmember melts were then mixed (in 10% intervals) producing mixed melt compositions. For these melts the composition of equilibrium olivines were

Fig. S5. Melt fraction and composition of experimental melts of pyroxenite and fertile peridotite. Temperatures for experimental runs of fertile peridotite (S2) are extrapolated to 3.5 GPa by using slope 100°C/GPa. Data for pyroxenite from Table S3. Crystalline phase coexisting with melt are: OI - olivine; Opx - orthopyroxene; Cpx - clinopyroxene; Ga - garnet. Blue and red ellipses indicate analyses averaged to calculate peridotite-derived and pyroxenite-derived endmembers respectively.

calculated using Herzberg's model (S5). The calculated Mn/Fe ratios of the olivines and the amounts of pyroxenitic endmember (X_{px}) yield a straight line:

$$X_{\text{px}} = 3.48 - 2.071 \times (100\text{Mn/Fe}) \quad [\text{S2}]$$

We used this equation to calculate the amount of pyroxenitic endmember for each average olivine composition in Table S2a.

The calculated endmember compositions are derived from experiments at high pressures and temperatures. Therefore, they are directly relevant primarily to thick-lithosphere settings, but we have applied them for all settings. Equivalent estimates for lower pressures and temperatures (1.0 GPa and 1300–1350°C) have been calculated using pMELTS (S6). This yielded similar degrees of melting and residual assemblages (50 to 60% of melting and low-Ca pyroxene dominated residue) as those derived from high pressure and temperature runs (Table S3). This gives us some confidence that the same Mn/Fe ratios can be applied to lower pressures, but experimental confirmation will be needed. Additional confidence in the results is derived from the observation that the extreme compositions observed in both MORB and WPM-thick settings match the calculated endmember compositions reasonably well.

Oceanic crust in magma sources. A final step is to estimate the actual amount of recycled oceanic crust (X_{crc}) from the determined proportion of pyroxenite-derived melt. This quantity is linked to the proportion of hybrid pyroxenite-derived melt (X_{px}) by the degree of melting of eclogite (F_e), the amount of eclogite-derived melt needed to produce hybrid pyroxenite from peridotite (X_e), and the degrees of melting of peridotite (F_{pe}) and pyroxenite (F_{px}) (S3):

$$X_{crc} = \frac{X_e}{F_e \left(\frac{1-X_{px}}{X_{px}} \frac{F_{px}}{F_{pe}} + \frac{1-F_e}{F_e} X_e + 1 \right)} \quad [S3]$$

Following assumption of Sobolev et al. (2005) (S3), we propose that the extent of melting of eclogites reaches a maximum of 50%. This limit is unlikely to be exceeded significantly during fractional melting, because this process removes Na (S7) and thereby renders the residue highly refractory. Therefore it is also not strongly dependent on the potential temperature of the rising mantle material. The amount of pyroxenite produced by reaction of the primary (eclogite-derived) melt with peridotite is prescribed by the stoichiometry of the reaction, which also yields proportions of the reactants of close to 50:50 (S3). For these, proportions, the amount of reaction pyroxenite equals the amount of initial eclogite. The melt fraction produced by the pyroxenite can be estimated at low pressure (1-2 GPa) by modeling using pMELTS software (S6), yielding a maximum of about 60 % for batch melting at 1 GPa and 1320 to 1350°C. At higher pressures (3.5 GPa) we must rely on the experimental data (Table S3, Fig. S5), which also yield a maximum melt fraction of about 50-60% for batch melting for 1540-1550°C.

These values will be significantly lower for fractional melting (S8), for the same reason as discussed for eclogite melting (i.e. early Na removal). Adopting an amount of 50 % pyroxenite melting will therefore result in a minimum estimate in the amount of recycled crust present. Finally, we estimate the melt fraction of peridotite using published models (S5) for MORB (10%), Iceland, as a proxy for the WPM-THIN group (20%), Hawaii, as proxy for the WPM-THICK group (10%) and Archaean komatiites ~40% (S9). This yields the following average estimates for the amounts of recycled oceanic crust in the mantle sources: 4% for MORB, 11% for WPM-THIN group, 16% for WPM-THICK group, and around 13% for Archean komatiites. According to (S10) the melt fraction of peridotite for Ontong Java high-Mg magmas corresponds to 30%, which yield the amount of recycled oceanic crust of 13-28% in the mantle source of these magmas.

Supporting Online References

- S1. E.J. Jarosevich, J.A. Nelen, J.A. Norberg, *Geostand. Newsl.* 4, 43 (1980).
- S2. M.J. Walter, *Journal of Petrology* 39, 29 (1998).
- S3. A.V. Sobolev, A.W. Hofmann, S.V. Sobolev, I.K. Nikogosian, *Nature* 434, 590 (2005).
- S4. K.P. Jochum et al., *Geostandards Newsletter—the Journal of GeoStandards and Geanalysis* 24, 87 (2000).
- S5. C. Herzberg, M.J. O'Hara, *Journal of Petrology* 43, 1857 (2002).
- S6. M.S. Ghiorso, M.M. Hirschmann, P.W. Reiners, V.C. Kress, *Geochemistry Geophysics Geosystems* 3 (2002).
- S7. T. Kogiso, M. Hirschmann, *Earth and Planetary Science Letters* 249, 188 (2006).
- S8. I. Kushiro, *Annual Review of Earth and Planetary Sciences* 29, 71 (2001).
- S9. N. Arndt, *Journal of Geophysical Research Solid Earth* 108 (2003).
- S10. J.G. Fitton, M. Godard, in *Origin and Evolution of the Ontong Java Plateau*, J.G. Fitton, J.J. Mahoney, P.J. Wallace, A.D. Saunders, Eds. (Geological Society, London, Special Publication, 229 London, 2004) pp. 151-178.
- S11. B. Sylvander, D.M. Christie, L.V. Danyushevsky, in *Eos* (1996), vol. 77, pp. F691.
- S12. M.R. Perfit et al., *Earth and Planetary Science Letters* 141, 91 (1996).
- S13. A.V. Sobolev, *Petrology* 4, 209 (1996).
- S14. V.S. Kamenetsky et al., *Earth and Planetary Science Letters* 160, 115 (1998).
- S15. V. Kamenetsky, *Earth and Planetary Science Letters* 142, 479 (1996).
- S16. A.P. Leroex, H.J. B. Dick, L. Gulev, A.M. Reid, A.J. Erlank, *Geochimica Et Cosmochimica Acta* 51, 541 (1987).
- S17. V.S. Kamenetsky et al., *Geology* 29, 243 (2001).
- S18. N.M. Sushchanskaya et al., *Geochemistry International* 43, 222 (2005), in Table S2b.
- S20. T. Elliott, J. Blécher-Tost, A. Heumann, G. Koetsier, V. Forjaz, *Geochimica Et Cosmochimica Acta* 71, 219 (2007).
- S21. S. Huang, M. Regelous, T. Thordarson, F.A. Frey, *Geochemistry Geophysics Geosystems* 6 (2005).
- S22. A.C. Kerr, R.W. Kent, B.A. Thomson, J.K. Seedhouse, C.H. Donaldson, *Journal of Petrology* 40, 873 (1999).
- S23. G.M. Yaxley, V.S. Kamenetsky, M.D. Norman, D. Francis, *Contributions to Mineralogy and Petrology* 148, 426 (2004).
- S24. L.M. Larsen, A.K. Pedersen, *Journal of Petrology* 41, 1071 (2000).
- S25. K.G. Cox, B.J. Jamison, *Journal of Petrology* 15, 269 (1974).
- S26. Y.G. Xu, S.L. Chung, B.M. Jahn, G.Y. Wu, *Lithos* 58, 145 (2001).
- S27. S.L. Chung, B.M. Jahn, *Geology* 23, 889 (1995).
- S28. M. Teklay, A.W. Hofmann, G.E. Brügmann, J.C. Lassiter, *Geochimica Et Cosmochimica Acta* 66, A767 (2002).
- S29. A.V. Sobolev, I.K. Nikogosian, *Petrology* 2, III (1994).
- S30. J.M. Rhodes, M.J. Vollinger, *Geochemistry Geophysics Geosystems* 5, Q03G13 (2004).
- S31. F.A. Frey et al., *Journal of Geophysical Research—Solid Earth and Planets* 96, 14347 (1991).
- S32. F.A. Frey, M.O. Garcia, M.F. Roden, *Geochimica Et Cosmochimica Acta* 58, 1441 (1994).
- S33. E.H. Haskins, M.O. Garcia, *Contributions to Mineralogy and Petrology* 147, 162 (2004).
- S34. M.D. Norman, M.O. Garcia, *Earth and Planetary Science Letters* 168, 27 (1999).
- S35. M.O. Garcia, D.J.P. Foss, H.B. West, J.J. Mahoney, *Journal of Petrology* 36, 1647 (1995).
- S36. V.V. Matviienko, O.G. Sorokhtin, *Okeanologiya* 38, 742 (1998).
- S37. A.A. Gurenko et al., *Chemical Geology* 233, 75 (2006).
- S38. A.A. Gurenko, T.H. Hansteen, H.U. Schmincke, in *Proceedings of the Ocean Drilling Program, Scientific Results* P. P.E. Weaver, H.U. Schmincke, J. V. Firth, W. Duffield, Eds. (1998), vol. 157, pp. 375-401.
- S39. N.T. Arndt, A.J. Naldrett, D.R. Pyke, *Journal of Petrology* 18, 319 (1977).
- S40. N.T. Arndt, *Journal of Petrology* 27, 279 (1986).
- S41. M.J. Bleekle et al., in *The geology of the Balingwe Greenstone Belt, Zimbabwe* M.J. Bleekle, E.G. Nisbet, Eds. (Balkema, Rotterdam, 1993) pp. 175-214.
- S42. N.T. Arndt, G.E. Brügmann, K. Lehner, C. Chauvel, B.W. Chappell, in *Geochemistry and Mineralization of Proterozoic Volcanic Suites* T.C. Pharaoh, R. D. Bleckinsale, D. Rickard, Eds. (Geol. Soc. Spec. Publ., 1987) pp. 133-145.
- S43. A.C. Kerr, *Lithos* 84, 77 (2005).

Table S2b. Locations (GPS coordinates) and description for Icelandic samples

Sample	Locality	Description	latitude	longitude
01-7	Reykjaness, Hafnabunga	Glassy olivine phryic picrite	N63°48.954'	W22°39.645'
03-102	Reykjaness, Lagafell	Glassy olivine phryic picrite	N63°52.906'	W22°32.611'
03-105	Reykjaness, Hafnabunga	Glassy olivine phryic picrite	N63°48.873'	W22°33.724'
01-15	Reykjaness, Sulur	Glassy olivine –phryic basalt	N63°54.094'	W22°32.558'
01-12	Reykjaness, Stafafell	Glassy olivine–plagioclase phryic picrite	N63°54.601'	W22°31.370'
01-8	Hengill, Midfell	Glassy olivine phryic picrite with rare plagioclase and clinopyroxene xenocrysts	N64°10.140'	W21°04.257'
01-10	Hengill, Midfell	Glassy olivine phryic picrite with rare plagioclase and clinopyroxene xenocrysts	N64°10.103'	W21°04.118'
01-19	Hengill, Maesfell	Glassy olivine phryic basalt with rare plagioclase and clinopyroxene xenocrysts	N64°06.252'	W21°04.744'
03-131	Kistufell	Glassy olivine phryic basalt	N64°47.605'	W17°13.745'
03-164	Kistufell	Glassy olivine phryic basalt	N64°46.918'	W17°12.713'
03-140	Kistufell	Glassy olivine phryic basalt	N64°47.651'	W17°12.202'
03-161	Kistufell	Glassy olivine phryic basalt	N64°47.808'	W17°13.957'
01-55	Theistareykir, Laufnandarhraun	Glassy olivine phryic picrite	N65°56.285'	W17°05.047'
01-57-4	Theistareykir, Laufnandarhraun	Glassy olivine phryic picrite	N65°55.791'	W17°04.463'
01-56-1	Theistareykir, Laufnandarhraun	Glassy olivine phryic picrite	N65°56.277'	W17°05.374'
01-41	Theistareykir, Theistareykjahráun	Glassy olivine phryic basalt	N65°57.547'	W17°04.120'
01-44	Theistareykir, Laufnandarhraun	Glassy olivine phryic picrite	N65°56.068'	W17°05.246'
01-56-2	Theistareykir, Laufnandarhraun	Glassy olivine phryic picrite	N65°56.277'	W17°05.374'
01-54	Theistareykir, Laufnandarhraun	Glassy olivine phryic picrite	N65°56.281'	W17°04.624'
01-51	Theistareykir, Langavilshraun	Glassy olivine phryic basalt with rare clinopyroxene phenocrysts	N65°56.058'	W16°52.282'
03-224	Snaefellsness, Enni	Glassy olivine phryic basalt	N64°54.146'	W23°45.776'
03-225	Snaefellsness, Sýchn-Raudamelur	Olivine phryic basalt	N64°52.296'	W22°17.368'
03-220	Snaefellsness, Ytri-Raudamelur	Olivine phryic basalt	N64°52.717'	W22°20.660'

Table S2a. Average compositions of most Mg-rich olivine phenocrysts (see text of paper for definition).

GROUP	Geodynamic setting	References	Sample	Geographic	Locality	N	Fo	Al ppm	Fepm	Mn ppm	Mg ppm	Ca ppm	Ni ppm	Cr ppm	100%MgFe	100%MnFe	100%NiFe	Al ppm	Fepm	Mn ppm	Mg ppm	Ca ppm	Ni ppm	Cr ppm	100%MgFe	100%MnFe	100%NiFe	
MORB	MORB	(S11)	113-16	Indian Ocean	105.25-E SEIR	24	69.49	270	799.79	1233	285627	1955	2109	359	1.617	0.712	0.569	0.135	2.494	0.05	4	422	234	9	27	5		
MORB	MORB	(S11)	145-3	Indian Ocean	116.72-E SEIR	9	69.90	298	77032	1224	285235	1761	2550	369	1.590	0.338	0.546	2.255	1.191	0.05	4	422	20	71	4	9		
MORB	MORB	(S11)	30-29*	Indian Ocean	121.26-E SEIR	10	69.60	236	79195	1250	285974	1843	2115	350	1.617	0.712	0.564	2.328	0.135	0.10	724	14	499	20	39	5		
MORB	MORB	(S11)	144-13	Indian Ocean	115.21-E SEIR	29	69.16	269	82335	1316	284471	1921	1933	363	1.599	0.677	0.557	2.334	0.171	0.05	6	377	8	265	20	39	5	
MORB	MORB	(S11)	16-10	Indian Ocean	127.74-E SEIR	24	69.60	272	78593	1239	285854	1921	2303	372	1.571	0.778	0.614	2.455	0.229	0.06	4	438	9	280	12	38	7	
MORB	MORB	(S11)	65-1	Indian Ocean	60.92-E SEIR	11	69.59	319	79556	1205	28733	1955	1972	259	1.556	0.662	0.545	2.646	0.239	0.05	10	417	8	287	10	29	4	
MORB	MORB	(S11)	65-22	Indian Ocean	56.63-E SEIR	10	68.18	213	865637	1453	287837	2163	1572	380	1.639	0.546	0.484	2.429	0.086	0.11	8	755	14	526	10	16	7	
MORB	MORB	(S11)	5-2	Indian Ocean	128.52-E SEIR	33	69.63	257	78238	1238	284600	1875	2393	364	1.582	0.669	0.633	2.395	0.207	0.04	3	307	6	235	3	17	2	
MORB	MORB	(S11)	16-19	Indian Ocean	127.59-E SEIR	18	68.40	235	87179	1357	289113	1920	1953	346	1.557	0.676	0.569	2.292	0.258	0.15	5	1112	18	675	21	48	6	
MORB	MORB	(S11)	54-1	Pacific Ocean	Garnet FZ	32	90.62	395	66527	1084	289751	2071	2817	480	1.557	0.940	0.654	2.975	0.259	0.02	10	171	3	169	3	38	11	
MORB	MORB	(S12)	54-1	Pacific Ocean	Silicic FZ	49	90.39	377	72454	1231	287261	1955	2861	137	413	1.531	0.998	0.651	2.739	0.250	0.03	4	191	3	201	2	15	1
MORB	MORB	(S12)	FZ-649-50	Atlantic Ocean	91-N MAR	36	89.75	301	78979	1213	283050	1953	2444	374	1.577	0.834	0.642	2.539	0.216	0.04	5	309	4	200	5	15	4	
MORB	MORB	(S12)	FZ-649-510	Atlantic Ocean	91-N MAR	28	88.76	302	84161	1235	282025	1832	2410	371	1.487	0.701	0.701	2.177	0.444	0.04	7	276	6	173	14	30	6	
MORB	MORB	(S12)	649(0)	Atlantic Ocean	91-N MAR	12	89.63	314	76344	1222	283379	1929	2501	444	1.560	0.653	0.665	2.472	0.239	0.05	7	410	6	334	18	20	2	
MORB	MORB	(S12)	649(0)	Atlantic Ocean	91-N MAR	10	88.67	310	83452	1240	288934	1875	2434	155	390	1.486	0.940	0.701	2.247	0.406	0.08	9	639	10	595	20	55	5
MORB	MORB	(S12)	AI-50, Sf9, D9, q-20	N. Atlantic	68-N MAR	55	69.61	312	76416	1184	293134	1856	2543	430	1.549	0.668	0.663	2.481	0.274	0.02	2	152	2	103	2	11	3	
MORB	MORB	(S12)	AI-32-11-92	N. Atlantic	62-N MAR	92	60.70	242	70116	1251	297618	2032	2461	502	1.642	0.627	0.580	2.898	0.082	0.01	5	109	5	97	9	7	5	
MORB	MORB	(S12)	AI-32-12-60	N. Atlantic	43-N MAR	70	60.63	240	68316	1124	288255	2340	2221	428	1.622	0.743	0.515	3.376	0.124	0.03	3	200	3	134	14	19	10	
MORB	MORB	(S12)	AI-32-12-610	N. Atlantic	43-N MAR	13	50.68	252	69594	1175	289550	2174	2391	510	1.705	0.765	0.528	3.153	-0.048	0.01	3	507	2	166	33	10	3	
MORB	MORB	(S12)	AI-32-12-2	N. Atlantic	43-N MAR	85	91.13	254	66583	1059	293972	2221	2339	531	1.639	0.762	0.523	3.321	0.110	0.03	4	132	27	18	10	10	3	
MORB	MORB	(S12)	AI-32-12-7	N. Atlantic	43-N MAR	55	91.03	213	67956	1115	302651	2393	2252	453	1.641	0.750	0.510	3.522	0.084	0.03	4	211	4	152	22	11	10	
MORB	MORB	(S12)	AI-32-11-178	N. Atlantic	43-N MAR	68	90.68	260	61555	1140	293957	2072	2479	521	1.581	0.827	0.572	2.956	0.070	0.03	5	202	3	126	12	15	6	
MORB	MORB	(S12)	Ch-31-Dorb 665	N. Atlantic	Famous	17	91.21	306	65586	1039	303957	2100	2721	592	1.561	0.935	0.603	3.154	0.251	0.09	9	670	12	371	6	81	6	
MORB	MORB	(S12)	CH-31-Dorb 13b-54-2	N. Atlantic	Famous	19	91.38	298	64581	1012	29730	2019	2820	595	1.587	0.879	0.568	3.127	0.237	0.07	10	523	9	265	7	89	8	
MORB	MORB	(S12)	ARF-73-10-03	N. Atlantic	Famous	62	91.30	295	64525	1039	289895	2346	2355	592	1.569	0.848	0.555	3.126	0.193	0.05	9	345	5	180	6	31	6	
MORB	MORB	(S16)	AG32-4-68	S. Atlantic	Bouvet	44	90.72	319	69596	1058	297851	2024	2653	450	1.554	0.891	0.623	2.861	0.264	0.04	7	270	5	165	7	41	10	
MORB	MORB	(S16)	AG-32-3-35	S. Atlantic	Bouvet	98	89.95	282	75474	1217	284027	1869	2239	427	1.612	0.761	0.576	2.476	0.144	0.04	4	264	4	156	4	40	6	
MORB	MORB	(S16)	AG-32-3-41	S. Atlantic	Bouvet	73	90.22	301	74170	1159	297481	1902	2432	474	1.616	0.818	0.606	2.566	0.132	0.02	5	149	3	122	10	35	7	
MORB	MORB	(S17)	51b-601	S. Atlantic	Romanche FZ	5	68.70	225	95849	1169	288230	1116	3478	536	1.204	1.232	1.226	1.120	0.99	0.05	5	308	6	345	11	24	22	
MORB	MORB	(S17)	13-124/9a	Atlantic Ocean	Romanche FZ	60	69.35	198	80892	1322	293514	2322	1959	139	270	1.648	0.677	0.547	2.958	0.070	0.03	3	230	4	206	6	13	1
MORB	MORB	(S17)	13-124/9c	Atlantic Ocean	Romanche FZ	58	88.98	198	827688	1357	296584	2455	1953	145	264	1.640	0.672	0.556	2.966	0.087	0.04	5	268	5	170	13	13	1
MORB	MORB	(S17)	13-124/9d	Atlantic Ocean	Romanche FZ	19	88.90	185	837965	1388	291945	2415	1872	143	1.656	0.641	0.537	2.681	0.053	0.06	7	416	4	229	31	18	2	
MORB	MORB	(S17)	13-124/9e	Atlantic Ocean	Romanche FZ	36	87.69	195	92539	1514	286753	1715	1704	322	1.636	0.724	0.670	1.654	0.095	0.02	4	102	3	160	4	10	2	
MORB	MORB	(S17)	13-124/9f	Atlantic Ocean	Romanche FZ	17	88.39	195	80132	1331	293545	2243	1785	141	260	1.651	0.757	0.542	3.048	0.044	0.06	6	476	9	339	11	12	2
MORB	MORB	(S17)	13-124/9g	Atlantic Ocean	Romanche FZ	21	69.23	201	81799	1338	292653	2402	1956	145	262	1.646	0.681	0.554	2.954	0.074	0.06	3	438	10	433	18	23	3
MORB	MORB	(S17)	13-11/1	Atlantic Ocean	Romanche FZ	21	88.11	240	82742	1358	297657	1705	1959	154	307	1.522	0.654	0.616	1.911	0.330	0.01	3	75	2	130	2	9	2
MORB	MORB	(S17)	13-11/2	Atlantic Ocean	Knipovich Edge	36	87.44	205	940563	1336	285613	1854	1653	164	341	1.420	0.550	0.517	1.970	0.542	0.05	3	341	6	219	6	11	1
MORB	MORB	(S17)	13-12/55	Atlantic Ocean	Romanche FZ	52	50.55	263	70926	1193	285461	2433	2279	130	356	1.636	0.770	0.670	1.571	0.18	0.01	3	253	0	1571	18	8	7
WPH-THIN	WPH-THIN	(S19)	0-1	Atlantic Ocean	Romanche FZ	13	89.34	211	75948	1314	294569	2355	147	283	1643	0.707	0.555	0.565	2.956	0.080	0.03	5	562	6	34	7	34	7
WPH-THIN	WPH-THIN	(S19)	0-13/14	Atlantic Ocean	Iceland	2	68.27	184	87742	1448	287388	1833	1501	142	284	1.651	0.522	0.458	2.146	0.064	0.08	0	653	0	39	11	8	17
WPH-THIN	WPH-THIN	(S19)	0-14	Arctic ocean	Knipovich Edge	31	87.55	213	93547	1512	285852	1813	1775	155	288	1.616	0.619	0.578	1.938	0.136	0.13	4	350	4	350	4	35	8
WPH-THIN	WPH-THIN	(S19)	0-15	Arctic ocean	Iceland	17	87.42	219	94211	1524	285900	1824	1747	157	291	1.618	0.613	0.578	1.936	0.132	0.13	5	695	5	357	7	16	8
WPH-THIN	WPH-THIN	(S19)	0-16	Arctic ocean	Iceland	51	90.22	344	74156	1475	287653	2355	1767	161	357	1.686	0.646	0.627	1.948	0.148	0.13	3	252	4	217	11	12	9
WPH-THIN	WPH-THIN	(S19)	0-16	Arctic ocean	Iceland	31	90.06	355	70700	1142	289521	2420	2520	549	1.614	0.643	0.597	1.447	0.141	0.05	14	362	7	254	17	23	16	
WPH-THIN	WPH-THIN	(S19)	0-16	Arctic ocean	Iceland	65	90.17	314	74317	1175	286502	2306	249															

GROUP	Geodynamic setting	References	Sample	Geographic	Locality	N	Fo	Al ppm	Fe ppm	Mn ppm	Mg ppm	Ca ppm	Ni ppm	Cu ppm	Cr ppm	100Mn/Fe	100Fe/Mg	Ni/Fe/Mg	Y/Fe	Y/Co	100Ca/Fe	Xpx/Mn/Fe	STE	Al ppm	Fo ppm	Mn ppm	Ca ppm	Ni ppm	Cr ppm	Ca ppm								
WPA+THICK	UP	unpub	SU-50	Sibera, Novosibirsk	Gudchinskaya unit	22	60.60	163	1400	939	1681	255505	1933	3017	327	1.267	1.176	1.648	1.378	0.683	0.07	3	50.1	6	341	7	19	6	341	7	19	6						
WPA+THICK	UP	(S28)	AK-31	Africa, Afar	Zaw-Helkelti, Emba Tekera, Eritrea	5	87.10	374	95459	139	2112	169	371	1.432	0.745	0.16	0.16	0.033	0.03	0.516	0.07	31	1.149	17	711	16	58	2	22	6	341	7	19	6				
WPA+THICK	UP	(S28)	AK-33	Africa, Afar	Zaw-Helkelti, Emba Tekera, Eritrea	9	68.34	475	75972	1186	291758	1691	212	1.58	480	1.483	0.743	2.364	0.412	0.10	0.17	711	9	421	6	26	3	25	3	12	6	341	7	19	6			
WPA+THICK	UP	(S28)	AG-10	Africa, Afar	Adi Ghebrey, Emba Tekera, Eritrea	1	88.30	513	870711	1266	285738	1938	252	154	493	1.477	0.697	0.780	2.193	0.423	0.00	0.00	0.00	0.00	0.00	0.07	0.8	483	8	259	8	35	3	15	6			
WPA+THICK	UP	(S28)	AG-15*	Africa, Afar	Adi Ghebrey, Emba Tekera, Eritrea	17	84.66	355	112774	1520	270733	1743	2154	182	295	1.356	0.795	0.687	1.546	0.673	0.07	0.07	0.07	0.07	0.07	0.02	0.3	104	11	5	3	15	3	15	6			
WPA+THICK	OB	(S29)	RV-7	Indian Ocean	Reunion, Plaine de la Nègue	73	65.66	224	105445	1587	276506	1937	2377	329	1.486	0.653	1.894	0.405	0.02	0.02	0.02	0.02	0.02	0.02	0.02	0.02	0.02	0.02	0.02	0.02	0.02	0.02	0.02	0.02	0.02	0.02	0.02	
WPA+THICK	OB	(S29)	RY-11	Indian Ocean	Reunion, Plaine de la Nègue	13	69.82	262	77029	1125	257516	1675	2370	534	1.460	1.044	0.774	2.174	0.459	0.08	0.08	0.545	0.11	0.444	0.04	28	38	12	12	12	12	12	12	12	12	12	12	
WPA+THICK	OB	(S29)	OPF	Indian Ocean	Reunion, Plaine de la Nègue	82	63.98	185	116585	1656	270479	1988	2016	243	1.430	0.745	1.677	0.684	0.02	0.02	0.02	0.02	0.02	0.02	0.02	0.02	0.02	0.02	0.02	0.02	0.02	0.02	0.02	0.02	0.02	0.02	0.02	
WPA+THICK	OB	(S30)	IKI-22	Hawaii	Kilauea Iki	9	68.28	255	879557	1205	288325	1780	3059	161	600	1.370	1.061	0.933	2.023	0.645	0.13	0.16	0.957	0.12	441	10	49	3	17	3	17	3	17	3	17	3	17	3
WPA+THICK	OB	(S30)	IKI-44	Hawaii	Kilauea Iki	20	68.54	288	85800	1176	285577	1742	3210	153	614	1.371	1.112	0.954	2.030	0.643	0.05	0.05	0.954	0.05	368	5	319	12	33	2	6	6	3	15	3	15	3	
WPA+THICK	OB	(S30)	KG7-12	Hawaii	Kilauea Iki	34	87.81	236	91065	1259	285538	1686	169	544	1.382	1.021	0.930	2.050	0.621	0.05	0.05	0.955	0.05	365	6	207	20	17	1	7	1	7	1	7	1	7	1	
WPA+THICK	OB	(S30)	KG7-14b	Hawaii	Kilauea Iki	67	69.41	255	86651	1195	287459	1376	3023	161	607	1.379	1.051	0.911	1.559	0.627	0.03	0.03	154	4	220	7	14	1	7	1	7	1	7	1	7	1		
WPA+THICK	OB	(S30)	SR-17-9.0	Hawaii	Mauna Loa, HSDP-2	31	90.22	264	73484	988	298523	1352	3310	165	663	1.357	1.119	0.822	1.840	0.671	0.02	0.02	1.34	2	131	2	25	1	15	1	15	1	15	1	15	1		
WPA+THICK	OB	(S30)	SR-18-0	Hawaii	Mauna Loa, HSDP-2	19	90.63	257	71919	984	289311	1359	3018	161	600	1.370	1.061	0.933	2.023	0.645	0.02	0.02	1.34	2	131	2	25	1	15	1	15	1	15	1	15	1		
WPA+THICK	OB	(S30)	SR-19-0.2-0	Hawaii	Mauna Loa, HSDP-2	7	89.32	196	81136	1133	285956	1791	2883	584	1.333	0.974	0.782	2.201	0.599	0.13	0.13	0.932	0.20	675	118	143	14	14	14	14	14	14	14	14	14	14		
WPA+THICK	OB	(S30)	SR-98-23-3.0	Hawaii	Mauna Loa, HSDP-2	31	89.94	278	76562	1031	297832	1428	3028	710	1.346	1.010	0.930	2.050	0.621	0.03	0.03	1.318	2	153	2	20	17	1	7	1	7	1	7	1	7	1		
WPA+THICK	OB	(S30)	SR-98-25-3.0(h)	Hawaii	Mauna Loa, HSDP-2	60	69.75	299	769523	1045	298557	1386	3050	151	736	1.358	1.036	0.911	1.817	0.670	0.02	0.02	1.325	3	165	7	25	1	11	1	11	1	11	1	11	1		
WPA+THICK	OB	(S30)	SR-101-7.0	Hawaii	Mauna Loa, HSDP-2	50	90.00	318	74951	1045	295507	1385	3277	150	784	1.322	1.051	0.931	1.821	0.621	0.03	0.03	1.325	3	125	3	24	1	5	1	5	1	5	1	5	1		
WPA+THICK	OB	(S30)	SR-104-5.5	Hawaii	Mauna Loa, HSDP-2	33	88.69	276	77006	1054	297956	1405	30700	745	1.358	1.044	0.931	1.849	0.620	0.05	0.05	1.324	3	197	6	37	27	27	27	27	27	27	27	27	27	27		
WPA+THICK	OB	(S30)	SR-104-5.5(h)	Hawaii	Mauna Loa, HSDP-2	70	69.77	287	77197	1057	294744	1413	3279	144	735	1.370	1.065	0.937	1.977	0.630	0.03	0.03	1.325	3	149	3	13	1	8	1	8	1	8	1	8	1		
WPA+THICK	OB	(S30)	SR-113-6.5	Hawaii	Mauna Loa, HSDP-2	63	89.58	273	77943	1057	295157	1409	30702	568	1.357	1.020	0.930	1.973	0.623	0.03	0.03	1.325	3	153	2	10	5	5	5	5	5	5	5	5	5			
WPA+THICK	OB	(S30)	SR-1117-0	Hawaii	Mauna Loa, HSDP-2	13	69.67	305	764522	1046	286564	1397	3140	636	1.342	1.065	0.934	1.974	0.623	0.03	0.03	1.325	3	173	6	39	15	15	15	15	15	15	15	15	15			
WPA+THICK	OB	(S30)	SR-120-24.2.5	Hawaii	Mauna Loa, HSDP-2	35	89.65	263	795263	1025	297528	1429	32532	722	1.351	1.051	0.931	1.974	0.624	0.03	0.03	1.325	3	197	4	19	1	1	1	1	1	1	1	1	1	1		
WPA+THICK	OB	(S30)	SR-120-24.2.5(h)	Hawaii	Mauna Loa, HSDP-2	40	69.30	243	82393	1125	291274	1453	30655	150	734	1.349	1.020	0.931	1.975	0.620	0.03	0.03	1.325	3	217	3	21	9	9	9	9	9	9	9	9	9		
WPA+THICK	OB	(S30)	SR-13-10.0	Hawaii	Mauna Kea, HSDP-2	7	87.33	211	95193	1130	285497	2011	2815	428	1.376	0.986	0.939	1.977	0.633	0.03	0.03	1.325	3	149	3	13	1	8	1	8	1	8	1	8	1			
WPA+THICK	OB	(S30)	SR-134-2.6	Hawaii	Mauna Kea, HSDP-2	25	66.71	212	98979	1154	287042	2066	2725	172	405	1.370	0.931	0.931	1.977	0.634	0.03	0.03	1.325	3	270	19	13	2	9	9	9	9	9	9	9			
WPA+THICK	OB	(S30)	SR-135-6.1	Hawaii	Mauna Kea, HSDP-2	16	69.20	210	82032	1101	284768	1637	2879	552	1.377	0.932	0.932	1.978	0.630	0.03	0.03	1.325	3	261	21	12	12	12	12	12	12	12	12	12	12			
WPA+THICK	OB	(S30)	SR-139-4.5	Hawaii	Mauna Kea, HSDP-2	31	89.23	190	91454	1126	285526	1938	30555	548	1.375	0.917	0.933	1.978	0.634	0.03	0.03	1.325	3	267	14	19	7	7	7	7	7	7	7	7	7			
WPA+THICK	OB	(S30)	SR-139-9.5	Hawaii	Mauna Kea, HSDP-2	24	69.11	196	820634	1126	292120	1640	30737	595	1.372	0.954	0.935	1.979	0.634	0.03	0.03	1.325	3	223	21	23	13	13	13	13	13	13	13	13	13			
WPA+THICK	OB	(S30)	SR-144-2.0	Hawaii	Mauna Kea, HSDP-2	42	68.75	244	84807	1154	287265	1719	2851	484	1.361	0.930	0.934	1.980	0.635	0.03	0.03	1.325	3	223	20	20	14	14	14	14	14	14	14	14	14			
WPA+THICK	OB	(S30)	SR-145-2.5.6	Hawaii	Mauna Kea, HSDP-2	19	88.00	201	90074	1241	285150	1688	30305	627	1.351	1.014	0.930	1.981	0.630	0.03	0.03	1.325	3	347	20	40	16	16	16	16	16	16	16	16	16			
WPA+THICK	OB	(S30)	SR-148-6.5	Hawaii	Mauna Kea, HSDP-2	36	88.95	241	83748	1123	293397	1546	3210	487	1.375	0.917	0.933	1.981	0.634	0.03	0.03	1.325	3	352	6	214	16	26	11	11	11	11	11	11	11	11		
WPA+THICK	OB	(S30)	SR-157-6.1	Hawaii	Mauna Kea, HSDP-2	27	69.35	201	80222	1146	294247	1602	30598	165	513	1.330	1.057	0.934	1.982	0.634	0.03	0.03	1.325	3	236	10	49	2	11	11	11	11	11	11	11	11	11	
WPA+THICK	OB	(S30)	SR-169-2.6	Hawaii	Mauna Kea, HSDP-2	69.55	247	80726	1053	285534	1541	30340	152	556	1.330	1.043	0.934	1.983	0.635	0.03	0.03	1.325	3	211	9	14	1	6	6	30	8	30	8	30	8	30	8	
WPA+THICK	OB	(S30)	SR-170-12.2	Hawaii	Mauna Kea, HSDP-2	59	68.30	213	82271</td																													

GROUP	Geodynamic setting	References	Sample	Geographic	Locality	N	Fo	Al ppm	Fe ppm	Mn ppm	Cr ppm	Ni ppm	Cu ppm	Ca ppm	Mg ppm	Na ppm	Si ppm	Fe wt%	XpxMnFo	100Cr/Fe	100Mn/Mg	100Ni/Mg	100Mg/Fe	100Ca/Fe	100Mn/Fe	Al ppm	Fe ppm	Mn ppm	Cr ppm
WPM-THICK	OIB	(S38)	953C-93R-06-45-55	Atlantic Ocean	Gran Canaria	4	62.31	167	1269.22	1748	2610.52	1930	2485	187	219	1.356	0.952	1.227	1.497	0.674	0.20	12	1377	18	908	61	74	5	6
WPM-THICK	OIB	(S38)	953C-93R-18-24	Atlantic Ocean	Gran Canaria	5	87.75	181	91.951	1300	2854.05	1602	3239	168	416	1.49	1.135	1.039	1.749	0.544	0.18	13	1234	16	702	53	160	3	26
KOMMATITES	KOMMATITES	(S39)	MUN-24	Canada	Munro 2.7 Ga	65	92.34	392	5852.23	925	3070.10	1582	3316	1441	1.530	1.080	0.632	0.210	0.03	4	223	4	162	4	4	4	6		
KOMMATITES	KOMMATITES	(S39)	MUN-414	Canada	Munro 2.7 Ga	63	89.42	254	8023.18	1238	2848.87	1625	2942	732	1.543	0.993	0.600	0.266	0.03	3	205	4	166	5	5	5	8		
KOMMATITES	KOMMATITES	(S39)	Ch-111*	Canada	Munro 2.7 Ga	32	88.62	299	8450.03	1339	2820.33	1645	3034	791	1.579	1.035	0.678	1.940	0.212	0.04	5	327	7	214	8	6	6	16	
KOMMATITES	KOMMATITES	(S40)	M-626	Canada	Aleto 2.7 Ga	11	92.61	334	5515.32	652	3055.10	1490	3461	1299	1.564	1.116	0.617	2.703	0.243	0.10	7	772	13	474	7	10	20	20	
KOMMATITES	KOMMATITES	(S40)	M-767	Canada	Aleto 2.7 Ga	6	93.53	350	4882.29	601	3132.37	1484	3481	1368	1.507	1.111	0.554	2.978	0.155	0.14	14	1032	13	575	10	41	30	30	
KOMMATITES	KOMMATITES	(S40)	M-866	Canada	Aleto 2.7 Ga	33	94.30	421	4381.91	719	3159.79	1484	3353	1263	1.638	1.061	0.466	3.381	0.091	0.05	9	404	5	274	5	6	6	20	
KOMMATITES	KOMMATITES	(S41)	MZ-4	Zimbabwe	Bellingsve 2.7 Ga	9	92.60	361	5337.73	885	3071.69	1494	3630	123	1.327	1.571	1.182	0.666	0.230	0.11	10	796	13	477	6	8	2	32	
KOMMATITES	KOMMATITES	(S42)	G-21	Canada	Gilmour 1.5 Ga	15	92.03	359	6094.91	948	3059.02	1782	3351	1055	1.559	1.095	0.667	2.897	0.256	0.09	9	626	9	327	11	18	25	25	
KOMMATITES	KOMMATITES	(S42)	G-18	Canada	Gilmour 1.5 Ga	2	91.63	352	6256.61	968	3058.04	1787	3304	1071	1.547	1.060	0.676	2.856	0.278	0.36	3	2662	46	1468	14	35	35	35	
KOMMATITES	KOMMATITES	(S42)	G-15	Canada	Gilmour 1.5 Ga	63	88.74	222	6527.77	1281	2924.37	1796	2190	652	1.533	0.749	0.639	2.108	0.371	0.04	3	263	4	156	2	3	5	5	
KOMMATITES	KOMMATITES	(S42)	G-5a	Canada	Gilmour 1.5 Ga	70	88.67	244	8562.37	1284	2817.70	1793	2617	675	1.500	0.697	0.768	2.084	0.377	0.03	6	209	3	124	3	5	9	9	
KOMMATITES	KOMMATITES	(S43)	GOR-94-19	Georgia	Gorgonia 0.9 Ga	71	91.44	549	6465.07	1051	3045.62	2140	3593	920	1.626	1.196	0.773	3.313	0.115	0.02	4	126	2	117	2	5	5	5	
KOMMATITES	KOMMATITES	(S43)	GOR-94-35	Georgia	Gorgonia 0.9 Ga	13	92.58	533	5677.70	930	3083.31	2120	3447	1167	1.638	1.119	0.635	3.734	0.090	0.08	10	613	11	396	10	16	41	41	
KOMMATITES	KOMMATITES	(S43)	GOR-94-34	Georgia	Gorgonia 0.9 Ga	27	91.50	473	6476.94	1042	3032.02	2274	3247	1003	1.609	1.071	0.684	3.511	0.150	0.05	12	402	7	256	12	12	15	15	
KOMMATITES	KOMMATITES	(S43)	GOR-94-32	Georgia	Gorgonia 0.9 Ga	18	92.70	544	5462.32	907	3059.20	2121	3482	1195	1.661	1.139	0.622	3.862	0.043	0.07	16	527	9	266	12	10	29	29	

Notes for Table S2a. Concentrations and standard errors of mean (S.E.) are shown for elements in ppm and for Fo in mol%.

N-number of averaged high-Mg olivines (see text for definition). Samples marked (i) and (ii) represent different compositional groups of olivine within the same sample. Samples marked (n) represent an additional independent population of olivines analyzed for the same sample. References include samples description, unpubl.-unpublished. * Ontong Java Plateau samples were arbitrary classified as WPM-THICK, but actually may belong to WPM-THIN at the time of formation.